arXiv:1106.3087v2 [astro-ph.CO] 2 May 2013

SPIDER: Probing the early Universe with a suborbital polarimeter

A. A. Fraisse,[1] **P. A. R. Ade,**[2] **M. Amiri,**[3] **S. J. Benton,**[4] **J. J. Bock,**[5,6] **J. R. Bond,**[7] **J. A. Bonetti,**[6] **S. Bryan,**[8] **B. Burger,**[3] **H. C. Chiang,**[1] **C. N. Clark,**[9] **C. R. Contaldi,**[9] **B. P. Crill,**[5,6] **G. Davis,**[3] **O. Doré,**[5,6] **M. Farhang,**[7,10] **J. P. Filippini,**[5] **L. M. Fissel,**[10] **N. N. Gandilo,**[10] **S. Golwala,**[5] **J. E. Gudmundsson,**[1] **M. Hasselfield,**[3] **G. Hilton,**[11] **W. Holmes,**[6] **V. V. Hristov,**[5] **K. Irwin,**[11] **W. C. Jones,**[1] **C. L. Kuo,**[12] **C. J. MacTavish,**[13] **P. V. Mason,**[5] **T. E. Montroy,**[8] **T. A. Morford,**[5] **C. B. Netterfield,**[4,10] **D. T. O'Dea,**[9] **A. S. Rahlin,**[1] **C. Reintsema,**[11] **J. E. Ruhl,**[8] **M. C. Runyan,**[5] **M. A. Schenker,**[5] **J. A. Shariff,**[10] **J. D. Soler,**[10] **A. Trangsrud,**[5] **C. Tucker,**[2] **R. S. Tucker,**[5] **A. D. Turner,**[6] **and D. Wiebe**[3]

[1]Department of Physics, Princeton University, Princeton, NJ, USA

[2]School of Physics and Astronomy, Cardiff University, Cardiff, UK

[3]Department of Physics and Astronomy, University of British Columbia, Vancouver, BC, Canada

[4]Department of Physics, University of Toronto, Toronto, ON, Canada

[5]Department of Physics, California Institute of Technology, Pasadena, CA, USA

[6]Jet Propulsion Laboratory, Pasadena, CA, USA

[7]Canadian Institute for Theoretical Astrophysics, University of Toronto, Toronto, ON, Canada

[8]Department of Physics, Case Western Reserve University, Cleveland, OH, USA

[9]Theoretical Physics, Blackett Laboratory, Imperial College, London, UK

[10]Department of Astronomy and Astrophysics, University of Toronto, Toronto, ON, Canada

[11]National Institute of Standards and Technology, Boulder, CO, USA

[12]Department of Physics, Stanford University, Stanford, CA, USA

[13]Kavli Institute for Cosmology, University of Cambridge, Cambridge, UK

E-mail: afraisse@Princeton.EDU

Abstract. We evaluate the ability of SPIDER, a balloon-borne polarimeter, to detect a divergence-free polarization pattern (B-modes) in the cosmic microwave background (CMB). In the inflationary scenario, the amplitude of this signal is proportional to that of the primordial scalar perturbations through the tensor-to-scalar ratio r. We show that the expected level of systematic error in the SPIDER instrument is significantly below the amplitude of an interesting cosmological signal with $r = 0.03$. We present a scanning strategy that enables us to minimize uncertainty in the reconstruction of the Stokes parameters used to characterize the CMB, while accessing a relatively wide range of angular scales. Evaluating the amplitude of the polarized Galactic emission in the SPIDER field, we conclude that the polarized emission from interstellar dust is as bright or brighter than the cosmological signal at all SPIDER frequencies (90 GHz, 150 GHz, and 280 GHz), a situation similar to that found in the "Southern Hole." We show that two ~ 20-day flights of the SPIDER instrument can constrain the amplitude of the B-mode signal to $r < 0.03$ (99% CL) even when foreground contamination is taken into account. In the absence of foregrounds, the same limit can be reached after one 20-day flight.

Contents

1 Introduction

Over the past decade, our understanding of cosmology has been revolutionized by ever more precise measurements of the temperature and of the polarization of the Cosmic Microwave Background (CMB). The first-year *WMAP* data provided the first full-sky characterization of the CMB temperature anisotropies, first detected by *COBE* [1] and mapped with high fidelity by BOOMERANG [2], over a range of angular scales that allowed for the derivation of stringent cosmological constraints [3]. These constraints were further strengthened by *WMAP*'s full-sky measurement of a curl-free polarization pattern (*E*-mode) in the CMB sky [4], a pattern first detected from the ground by DASI [5]. Many other CMB experiments, both ground-based and balloon-borne, have provided complementary measurements, which made it possible to study physics poorly constrained by *WMAP* alone. This is the case of QUaD [6] and ACBAR [7], whose data combined with *WMAP*'s enabled the convincing detection of the effect of primordial helium on the CMB temperature power spectrum [8], thereby opening a new window on big bang nucleosynthesis. ACT [9] and SPT [10] have provided temperature data down to arcminute scales, probing the CMB power spectrum up to the seventh acoustic peak, while BICEP [11] first detected the $\ell \sim 100$ acoustic peak in the *E*-mode power spectrum, a detection later confirmed by QUIET [12].

Remarkably, the six parameters of the simple flat, power-law ΛCDM model are sufficient to fit not only all the available CMB temperature and polarization data, but also a wealth of other cosmological probes, such as distance measurements from Baryon Acoustic Oscillations [BAOs, 13], and Hubble constant measurements from Cepheids [14]. Although it is *possible* to fit more parameters to the data, there is no indication that any are *needed* [8]. The inflation paradigm, which postulates the existence of a period of accelerated expansion in the early Universe, is the cornerstone of this very successful model [15]. Not only does it explain

the flatness and the homogeneity of the Universe, it also provides a natural mechanism to generate the primordial Gaussian density fluctuations that left their imprint in the form of anisotropies in the CMB temperature and in the distribution of the large-scale structure we observe today. However, although inflation is *consistent* with current observational data, there is no direct *evidence* to date in favor of this paradigm over its viable alternatives. The ekpyrotic scenario [for a review, see, e.g., 16] is arguably the best motivated alternative to inflation. In addition to also being consistent with current data, it has the added benefit of naturally avoiding some of the theoretical complications that one encounters when building an inflationary model.

The predictions of the ekpyrotic scenario and of the inflationary paradigm differ in one major way. The latter generically predicts the existence of gravity wave perturbations in the early Universe, which would result in an observable divergence-free polarization pattern in the CMB (B-modes), whereas the former excludes the production of such perturbations at a detectable level [17]. B-modes therefore constitute an unambiguous signature of inflation. Moreover, the energy scale of inflation sets the amplitude of these tensor (gravity wave) perturbations relative to that of the scalar (density) perturbations in the form of the tensor-to-scalar ratio r. In addition to validating the inflationary paradigm, detecting B-modes would therefore determine the energy at which inflation occurs, which would remove the largest source of uncertainty in inflationary model building.

B-modes remain as yet undetected. BICEP [11] derived the strongest constraint on r directly from B-mode nondetection to date: $r < 0.72$ (95% CL). Using CMB temperature data from SPT, along with CMB temperature and polarization data from *WMAP* [8], distance measurements from BAOs [13], and recent constraints on the Hubble constant [14], [10] found an upper limit of $r < 0.17$ (95% CL). This constraint is about an order of magnitude above that necessary to rule out the simplest viable class of inflationary models [15].

The *Planck* satellite has already revolutionized our understanding of the sky at microwave to submillimeter wavelengths [18]. It has so far proven to be a remarkable machine to study the properties of the interstellar medium, and in particular of the emission from Galactic dust, which is expected to be the brightest polarized sky signal in all channels of *Planck*'s High Frequency Instrument (HFI). Even though *Planck*'s sensitivity will be sufficient to map the diffuse Galactic dust emission and constrain the amplitude of its polarized component, it will not be high enough to produce high signal-to-noise maps of this polarized emission at scales smaller than ~ 20 degrees. This in turn limits *Planck*'s ability to probe the cosmological B-mode signal beyond the large-scale reionization bump located below $\ell \sim 10$. Optimistic forecasts of *Planck*'s ability to detect or constrain B-modes have been published [e.g., 19]. However, two major assumptions are made in these studies: (1) that the *Planck* HFI is ideal at large angular scales ($1/f$ noise is for example ignored), and (2) that residuals after foreground removal are small enough that the induced bias on the determination of r is negligible. Although it is difficult to evaluate whether this latter assumption is reasonable, the former is most likely problematic (for an early review of the HFI noise, see [20]).

SPIDER [21] is a balloon-borne polarimeter designed to probe the polarization of the microwave sky with unprecedented sensitivity and fidelity. The Antarctic Long Duration stratospheric Balloon (LDB) platform provides a combination of long flight times, near-space optical backgrounds, and sensitivity to angular scales that are inaccessible from even the most favorable ground-based sites. By taking advantage of these observing conditions during two flights to be launched, respectively, in December 2013 and December 2015, SPIDER will
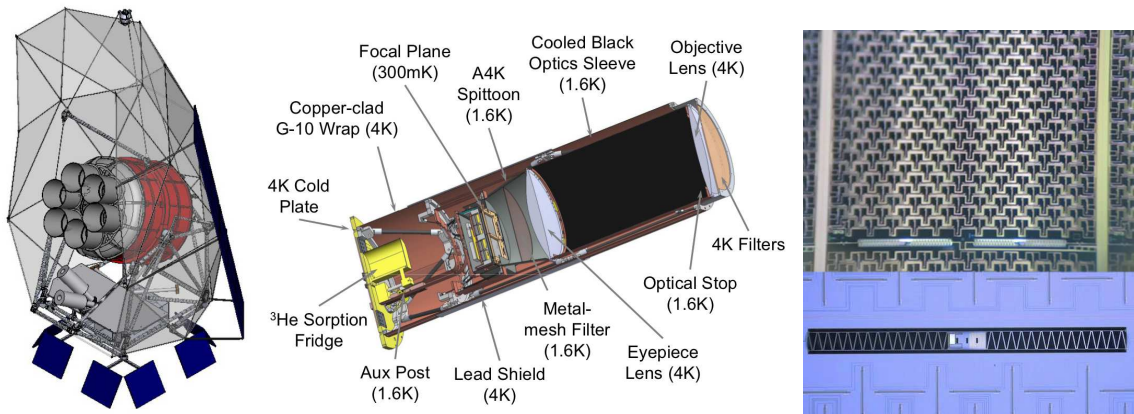
Figure 1 *Left:* Rendering of the SPIDER payload, showing the cryostat, surrounding frame, and sun shield. *Center:* Cross-section of the SPIDER telescope CAD model with key components labeled. *Top right*: Optical pixel, showing phased array of slot antennas feeding two TESs at bottom. *Bottom right*: Close-up of a single TES assembly, showing the TES island and the SiN thermal isolation legs. The meandered leg design allows for low thermal conductance in a narrow geometry.

produce high signal-to-noise polarized maps of 10% of the sky that are exceptionally clean of polarized Galactic emissions, with the goal of detecting and characterizing the $\ell \sim 80$ acoustic peak in the B-mode power spectrum for values of the tensor-to-scalar ratio r down to 0.03. In this paper, we review the current status of the SPIDER experiment, and present our observing plans to achieve this science goal.

This paper is organized as follows. In Section 2, we briefly describe the SPIDER instrument, and evaluate the level of B-mode contamination expected from known sources of systematic error. Section 2.3 presents a detailed study of the impact of polarized sidelobes on our observations. The expected level of polarized Galactic foregrounds in the SPIDER field is summarized in Section 3, where we also present a model for the polarized emission from interstellar dust. In Section 4, we provide an overview of our observing strategy, along with a computation of SPIDER's filter transfer function F_ℓ. Section 5 details the reasoning that led to the selection of 90 GHz, 150 GHz, and 280 GHz as SPIDER's observing frequencies, and gives our expected constraints on r taking into account polarized foreground contamination. Our conclusions are summarized in Section 6.

2 The SPIDER instrument

2.1 Description

The SPIDER payload (Figure 1) consists of six monochromatic refracting telescopes derived from the design of the highly successful BICEP instrument. This compact, axisymmetric optical system greatly limits the opportunity for polarized systematics. The relatively small aperture ($\sim 30'$ beam FWHM at 150 GHz) allows relatively easy baffling of optical sidelobes while retaining sensitivity to the angular scales relevant to inflationary science. The far-field regime of the optics is also relatively nearby (~ 100 m), greatly simplifying optical characterization in the laboratory.

Table 1.   SPIDER observing bands, pixel and detector counts, and single-detector and single-telescope FPU sensitivities

Band Center [Bandwidth] (GHz)	Beam FWHM (arcmin)	Detector Count per FPU	Detector Sensitivity ($\mu K_{CMB}\sqrt{s}$)	FPU Sensitivity ($\mu K_{CMB}\sqrt{s}$)
90 [22]	49	288	150	10
150 [36]	30	512	150	7
280 [67]	17	512	380	18

Note. — Each FPU sensitivity is obtained by dividing the corresponding single-detector sensitivity by $\sqrt{N_{\rm det}}$, assuming a detector yield of 85%, slightly below the average of the delivered focal planes. The total experimental map depth at each frequency scales inversely as the square-root of the number of FPU·flights for that frequency. The quoted sensitivities at 90 GHz and 150 GHz are our current best estimate based on in-situ measurements of signal and noise using an aperture filling 4 K load. The 280 GHz sensitivity is scaled from the average in-flight sensitivity of BOOMERANG at 245 GHz and 345 GHz. All three bands cover frequency ranges over which atmospheric loading, as infered from [27], is minimal.

Each refractor illuminates a focal plane of large-format antenna-coupled transition-edge sensor (TES) arrays [22]. Each of a focal plane's optical pixels consists of two interpenetrating arrays of slot antennas sensitive to perpendicular polarization components. The power received by each antenna array is coupled to a dedicated TES through an inline band-defining microstrip filter. The antennas, filters and bolometers for hundreds of polarimetric pixels are fabricated photolithographically onto a single silicon tile, with no need for external feed horns or band-defining filters. The arrays are read out using a time-domain SQUID multiplexer system [23, 24]. Four such focal planes are currently in operation at the South Pole, as part of the BICEP2 instrument [25] and the Keck array [26].

SPIDER will deploy telescopes in three frequency bands centered at 90, 150 and 280 GHz. Table 1 lists some of the major characteristics of a single SPIDER receiver in each of these observation bands. These frequencies are chosen for their sensitivity to the CMB and to Galactic dust emission. Since all frequency-specific optical elements are fully contained within each telescope insert, SPIDER's frequency coverage is easily adjustable by swapping out one or more of these telescopes. This modularity gives SPIDER a great deal of flexibility in choosing an optimal frequency coverage for each flight. Band selection is discussed further in Section 5.

The six receivers are housed within a shared ~ 1300 L liquid helium cryostat, with sub-Kelvin cooling for each focal plane provided by a dedicated ^{3}He sorption refrigerator. The cryostat is supported below the balloon within a lightweight carbon-fiber gondola frame, derived from the BLAST [28] design. A reaction wheel allows the payload to scan in azimuth, while the elevation of the inner frame is adjustable with a simple linear actuator similar to the BOOMERANG [29] design. Pointing information is provided by two tracking star cameras, one fixed star camera, rate gyroscopes, differential GPS, and a sun sensor. Extensive sun shielding and baffling, combined with the relatively small optical apertures of the SPIDER telescopes, allows the instrument to scan close to the Sun for increased sky coverage.

The design of SPIDER has been extensively optimized to take full advantage of the low millimeter-wave backgrounds available from a stratospheric balloon platform, as well as to ameliorate polarized systematics to the level needed to characterize B-mode polarization. SPIDER employs detector arrays very similar to those successfully fielded in BICEP2 and the Keck array, but tuned for much lower noise-equivalent temperatures. Extensive filtering

Table 2. Expected sources of systematic error for SPIDER

Source	Target	$\mathcal{C}_{100}^{\mathrm{residual}}/\mathcal{C}_{100}^{BB}$	Current Status
Relative gain uncertainty: $\Delta(g_1/g_2)/(g_1/g_2)$	0.5%	17%	0.1% Achieved by BOOMERANG[a]
Differential pointing: $(\mathbf{r}_1 - \mathbf{r}_2)/\sigma$	5%	20%[†,*]	2.4% Measured in SPIDER
Differential beam size: $(\sigma_1 - \sigma_2)/\sigma$	0.5%		0.3% Measured in BICEP2[d]
Differential ellipticity: $(e_1 - e_2)/2$	0.6%		0.15% Measured in BICEP2
Absolute polar angle calibration: $\Delta\Psi_{\mathrm{abs}}$	1°	17%	0.7° Achieved by BICEP[b]
Relative polar angle knowledge: $\Delta\Psi_{\mathrm{rel}}$	1°	6%	0.1° Achieved by BICEP[b]
Telescope pointing uncertainty: $\Delta\mathbf{b}$	10′	6%	2.4′ Achieved by BOOMERANG[c]
Beam centroid uncertainty: $\Delta\mathbf{c}$	1.2′	12%	Achieved by BICEP[b]
Polarized sidelobes (150 GHz): G_{s}	−17 dBi[‖]	8%[‡]	Achieved by BICEP[b]
Optical ghosting: G_{r}/G_0	−17 dB	6%	Achieved by BICEP2[d]
HWP differential transmission: p	0.7%	10%[†]	Achieved by SPIDER[e]
Magnetic shielding at focal plane: Φ_{s}	10 $\mu K_{\mathrm{CMB}}/B_e$	3%[†]	Achieved by SPIDER[f]

[‖]Gain at 30° from the telescope boresight
[*]Amplitude of the residual for the three sources of systematic error combined
[†][33]; [‡]This paper (see Section 2.3); [a][29]; [b][34]; [c][35]; [d][36]; [e][30]; [f][31]

Note. — The target for each parameter is set so that the maximum false B-mode signal is less than the B-mode power spectrum at $\ell = 100$ for $r = 0.03$. The third column provides the expected level of residual for each systematic effect if the target is exactly met [unless otherwise noted, numbers are from 37]. The conventions for beam-related systematic errors follow those in [38]. B_e is the strength of the Earth's magnetic field. The optical ghosting simulations of [37] primarily probe $E \to B$ contamination and not the potentially more important $T \to B$ contribution that would be expected given nontrivial polarization of the optical ghosts. We are currently revisiting the ghosting simulations to incorporate our knowledge of their polarized response. Given the frequency dependence of the foreground emission (see Section 3.1), requirements for polarized sidelobes at 150 GHz are sufficient for observations at 90 and 280 GHz. The *Current Status* column indicates whether each target is met given current measurements (for SPIDER, this corresponds to lab studies). When no reference is given, the current status is based on unpublished measurements. Adding all systematic errors in quadrature gives a total false signal of $\sim$37% of the $r = 0.03$ B-mode signal at $\ell = 100$.

and cold (< 3 K) baffling within each instrument greatly reduces stray photon loading on the bolometers. SPIDER's simple, telecentric optics limit the contribution of polarized optical sidelobes. A 4 K half-wave plate at the aperture of each telescope [30] is stepped in orientation periodically throughout the observation period in order to modulate the polarization signal of the sky with respect to any polarized instrumental systematics. These systematics have already been characterized extensively during optical testing of the first SPIDER telescopes and through operation of similar technology at the South Pole. Tolerances and achieved performance are described in more detail in Section 2.2. For a more detailed description of the SPIDER instrument, we refer the reader to [21, 31, 32].

2.2 Systematics review

Precise control of instrument systematics is crucial for achieving SPIDER's science goals. Table 2 summarizes our current understanding of a variety of sources of systematic error, including gain uncertainty, pointing and beam effects, half-wave plate nonidealities, and sensitivity to the Earth's magnetic field. We characterize each systematic effect using a suite of simulations with no input B-mode power, by assuming a target level of control over the relevant parameters, and measuring the level of the resulting false B-mode signal at $\ell = 100$. The design requirement is to reduce systematic error to a level of $(43 \text{ nK})^2$, the value of the primordial $r = 0.03$ B-mode power spectrum at $\ell = 100$ in units of $\ell(\ell + 1)C_\ell/(2\pi)$.

In most cases, the target values for each parameter are derived from a well-established simulation pipeline described in detail in [37] and [33]. The simulations include a detailed model of polarized Galactic dust emission, which interacts nontrivially with instrumental effects. The aim of these simulations is to quantify the extent to which a false B-mode signal is produced from systematics that induce $I \to Q, U$ or $Q \leftrightarrow U$ mixing, when no attempt is made to correct for them. These simulations assume a scan strategy and observing region that differ from the current baseline. However, internal simulations done using the McMurdo observing strategy described in Section 4.1 suggest that science requirements will be comparable. Further simulations are ongoing.

Many of the targets listed in Table 2 for systematics related to design elements common to both BICEP and SPIDER have been met by the former [34], which ensures that SPIDER is in a position to do so as well. Additional sources of systematic error due to half-wave plate nonidealities and magnetic field pickup are investigated in detail in [33]. In both cases, we find that the level of B-mode contamination is small compared to the $r = 0.03$ inflationary signal, even without special effort to correct for these systematics.

SPIDER's control of systematic errors is further enhanced by the use, with each telescope, of a rotating half-wave plate that is periodically stepped so that the same patch of sky is observed at multiple orientation angles, thereby augmenting the natural angular modulation due to the motion of the sky. This homogenizes the statistical noise in polarization and provides powerful rejection of a variety of instrumental systematics. By locating the half-wave plate skyward of the telescope aperture, we ensure that only the sky signal is modulated and that the effects of beam mismatches between detectors within a pair are greatly reduced.

Gain drifts contribute significantly to the systematics budget. BOOMERANG achieved a relative gain uncertainty less than 0.1%, a level five times smaller than the target established for SPIDER in [37], using an on-board calibration lamp [29]. We expect SPIDER to reach a similar level of control using regular modulations of the detector bias currents. This technique is currently undergoing laboratory tests. A BOOMERANG-style calibration lamp is also an option, pending the results of these studies.

Thermal fluctuations within the instrument will inevitably create a signal in the SPIDER bands. Changes in focal plane temperature (e.g., with payload altitude) can mimic a sky signal by changing the power flow through the bolometer support membranes. SPIDER's TES bolometers self-heat to a temperature largely independent of that of the focal plane, rendering them less sensitive to such fluctuations than a comparable semi-conductor bolometer. Since the monolithic fabrication of each detector array ensures good uniformity in thermal response within each polarization pair, such fluctuations do not propagate as strongly into a false polarization signal. A passive thermal filter, consisting of stainless steel heat capacity blocks between the detectors and thermal strap, supresses any thermal fluctuations on time scales comparable to the scan (by a factor of ~ 20 dB at 30 mHz).

Since about 25% of each beam terminates on the optical stop, changes in the stop temperature will also mimic a sky signal. Essentially all such internal sidelobes terminate on the cooled (~ 1.8 K) optics sleeve, however, whose low temperature limits the sensitivity of the bolometers to such drifts.

We report on simulations specifically designed to evaluate the level of the contamination expected from polarized sidelobes in the next section.
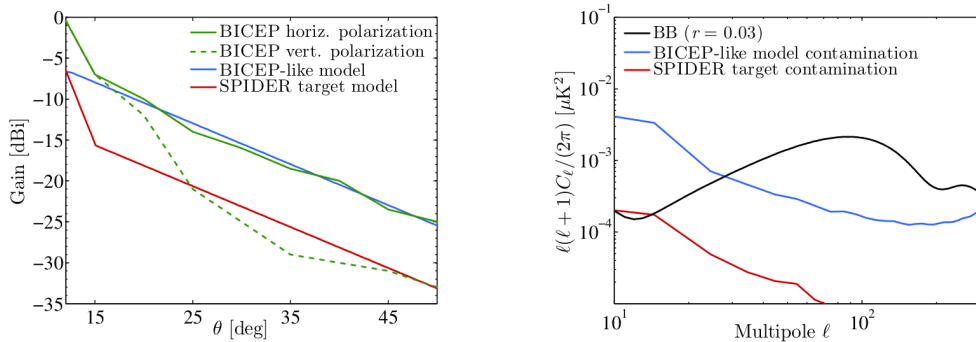
Figure 2 *Left:* Polarized sidelobe profiles measured at 150 GHz in BICEP (green) and models used in the analysis presented in Section 2.3. We consider two models: a sidelobe profile comparable to BICEP's (blue), and SPIDER's target profile, which assumes an additional 10 dB attenuation starting at 12° from the telescope boresight (red). *Right: B*-mode power spectra of the sidelobe pickup obtained with the sidelobe profiles shown in the left panel. The $r = 0.03$ primordial B-mode power spectrum is shown for comparison. The contamination is well below the cosmological signal at $\ell = 100$ for both profiles. However, the BICEP-like model leads to substantial contamination at large angular scales ($\ell \lesssim 25$). SPIDER's target profile ensures that the false B-mode signal is comparable to or fainter than the cosmological signal at low multipoles, and negligible at $\ell \sim 80$, where the primordial B-mode power spectrum peaks.

2.3 Polarized sidelobes

Coupling through the beam sidelobes to emission from the Sun, the Earth, and the Galactic plane will produce a spurious polarized signal. In order to establish mission requirements for SPIDER's sidelobe response, we convolve a polarized sidelobe profile with a temperature map of the Galactic emission at 150 GHz based on the sky model developed in [33] and discussed further in Section 3.2. Because of its complex morphology and proximity to SPIDER's observing region, the Galaxy is indeed expected to represent the most significant source of contamination on the scales of interest. SPIDER's optical system is a cryogenic refracting telescope, based on that developed for BICEP. Unlike BICEP, SPIDER employs a conical baffle with its base located inside the cryostat and extending roughly 0.5 m out from the surface of the vacuum vessel. The rim of the baffle is asymmetric to prevent direct illumination of the half-wave plate by the balloon and the Earth's limb, and intercepts the field of view between 10°–12°, in contrast with the 15° cutoff angle for the BICEP telescope forebaffle. SPIDER's main beam and near (2°–12°) sidelobe profiles are informed by a physical-optics model of the ideal optical chain internal to the cryostat, which includes both lenses and the half-wave plate. Accurately modeling SPIDER's far (> 12°) sidelobes requires a complete simulation of the optical system including sun shield, baffle, gondola, and balloon that has yet to be performed. Instead, we first model SPIDER's far sidelobe profile as a power law out to 50°, where the beam is truncated. This model is consistent with measurements of BICEP's polarized sidelobe response [34], which is representative of BICEP's relatively less restrictive forebaffle. The profile we use is shown in the left panel of Figure 2.

The B-mode power spectrum derived from the sidelobe model described above is shown in the right panel of Figure 2. Compared to the primordial $r = 0.03$ B-mode signal, it is over 12 times fainter at $\ell = 100$, while it is significantly brighter at large angular scales ($\ell \lesssim 25$).

Unsurprisingly, the BICEP forebaffle, which was designed to provide rejection at the level of $r \sim 0.1$ while observing at relatively high Galactic latitudes, does not provide sufficient rejection of the foreground signal for SPIDER's large-scale measurements. By adding ~ 10 dB of attenuation beyond $12°$ off axis as shown in the left panel of Figure 2, the expected sidelobe signal decreases to a level near or below the $r = 0.03$ B-mode spectrum at all scales of interest. The contamination is then over an order of magnitude fainter than the cosmological signal at $\ell \sim 30$, and entirely negligible at the $\ell \sim 80$ peak (see Figure 2). Although further testing is required to demonstrate that SPIDER's baffle will provide the required factor of ten improvement over the BICEP measurement, it appears to be well within reach. For instance, a simple diffraction calculation shows that adding a one-inch diameter diffraction edge on the sun shield at the edge of the baffle aperture leads to a gain at $12°$ off axis that is ~ 20 dB lower than in the BICEP-like model. This additional attenuation remains above 10 dB all the way to $50°$ off axis.

3 Galactic foregrounds

3.1 Polarized foregrounds in the SPIDER field

During its first two flights, SPIDER will map the microwave sky at frequencies ranging from 90 GHz to 280 GHz. At 90 GHz, the large-scale ($\ell \lesssim 10$) polarized emission from interstellar dust is expected to be at least an order of magnitude brighter than the $r = 0.03$ primordial B-mode signal that SPIDER aims to detect [39]. At smaller scales, the angular power spectrum of the polarized dust emission appears to be compatible with the power-law dependence $\mathcal{C}_\ell^{\mathrm{dust}} \propto \ell^{-2.6}$ [40], which results in its amplitude being comparable to that of our target B-mode signal at $\ell \sim 40$. Models indicate that this multipole dependence might break down in favor of a steeper decline at multipoles higher than $\sim 10^3$. Assuming that the polarized emission from interstellar dust obeys the same frequency dependence as its total emission, these results can be extrapolated to higher frequencies using the best-fit FDS model [41]. The resulting angular power spectra are ~ 9 and $\sim 5 \times 10^2$ times higher than the 90 GHz signal at 150 GHz and 280 GHz, respectively. Throughout this paper, we assume spinning dust emission to be unpolarized, consistent with theoretical expectations [see, e.g., 42].

Among other Galactic foregrounds, only synchrotron emission is expected to be significantly polarized at microwave frequencies. We use the *WMAP* 23 GHz data to evaluate the amplitude of the polarized Galactic synchrotron emission in the SPIDER region at frequencies ranging from 90 GHz to 280 GHz. The extrapolated signal is negligible both at 150 GHz and at 280 GHz compared to the $r = 0.03$ B-mode signal. At 90 GHz, its large-scale power spectrum is a factor of two higher than that of the target signal, but a factor of five lower than that of the polarized emission from interstellar dust. We find the multipole dependence of the polarized synchrotron emission to be well described by the power law $\mathcal{C}_\ell^{\mathrm{synchrotron}} \propto \ell^{-2.5}$ [compatible with *WMAP*'s full-sky estimate in 4], which brings this spectrum under that of the $r = 0.03$ B-mode signal by $\ell \sim 30$. At the $\ell \sim 80$ B-mode peak, this foreground is an order of magnitude fainter than the target signal. As a result, we do not expect the Galactic synchrotron emission to limit SPIDER's ability to detect B-modes at the $r = 0.03$ level.

Since the Galactic plane will be masked during the cosmological analysis, we do not consider the polarization of the free-free emission that might be induced by Thomson scattering at the edges of HII clouds [43]. Free-free emission is otherwise unpolarized.

Given the considerations in this section, we expect the polarized emission from interstellar dust to be the one Galactic foreground that will hinder SPIDER's ability to detect a

primordial B-mode signal. We show in Section 3.2 that it is possible to select observing fields accessible from a McMurdo flight in which the polarized emission from interstellar dust is up to an order of magnitude fainter than discussed above at all SPIDER frequencies. However, even with this reduced level of contamination, Galactic dust is still the dominant polarized sky signal at and above 90 GHz. Section 5 therefore addresses the question of how Galactic emission and cosmological signal can be separated given an appropriate combination of frequency bands. We describe the Galactic foreground model required for both these analyses in Section 3.2.

3.2 Model for the polarized emission from interstellar dust

A model of the sky that SPIDER will observe was presented in detail in [33]. In this section, we summarize the procedure followed to create a template of the polarized emission from interstellar dust that takes into account the three-dimensional Galactic structure.

The nonsphericity of interstellar dust grains and their ability to align with the Galactic magnetic field (hereafter, the Field) were first put forth in an effort to explain the polarization of starlight observed independently by Hiltner and by Hall [44, 45]. With its long axis preferentially aligned perpendicular to the Field [see, e.g., 46], a dust grain absorbs more radiation in the direction perpendicular to the local Field line than in the direction parallel to it. This results in a net linear polarization of the incident starlight in the direction parallel to the Field. The polarization of the emission from dust grains is the counterpart of this absorption phenomenon. As a result, the emission from interstellar dust is expected to be polarized perpendicularly to the sky-projected direction of the Field. ARCHEOPS and *WMAP* both detected the polarization of the Galactic dust emission at microwave frequencies with high significance [4, 47], and found degrees of polarization over the sky compatible with theoretical expectations [48]. However, neither experiment had the combination of resolution and sensitivity necessary to produce a map of this emission usable by SPIDER. As a result, we must rely on modeling to estimate the characteristics of the polarized emission from interstellar dust in the SPIDER field.

Despite tremendous recent progress in our understanding of the alignment of interstellar dust with the Galactic magnetic field [see, e.g., the review in 49], we are still far from a full theoretical understanding of this physical process. Modeling the polarized emission from Galactic dust therefore requires simplifying assumptions. It is customary to assume (i) that each grain is aligned with the Field with its long axis exactly (as opposed to preferentially) perpendicular to the field line; (ii) that, given a field strength, each grain has the same polarizing effect; and (iii) that the degree of polarization of the dust emission induced by a grain is proportional to the square of the magnetic field strength at the location of the grain. With these assumptions, and given a three-dimensional model of the dust distribution and of the Galactic magnetic field, we compute a full-sky template of the polarization fraction and angle of the Galactic dust emission. Details of the three-dimensional models and of the calculation performed to derive the template are provided in [33]. Since the magnetic field model includes a small-scale turbulent component, the resulting depolarization effect is taken into account. The overall amplitude of the template for the polarized fraction of the Galactic dust emission is a free parameter, which we set to match the average value of 3.6% derived by *WMAP* outside of the Galactic plane [50]. We obtain polarized intensity maps by multiplying the template by the dust intensity map from [41], using their model 8 to account for its frequency dependence.
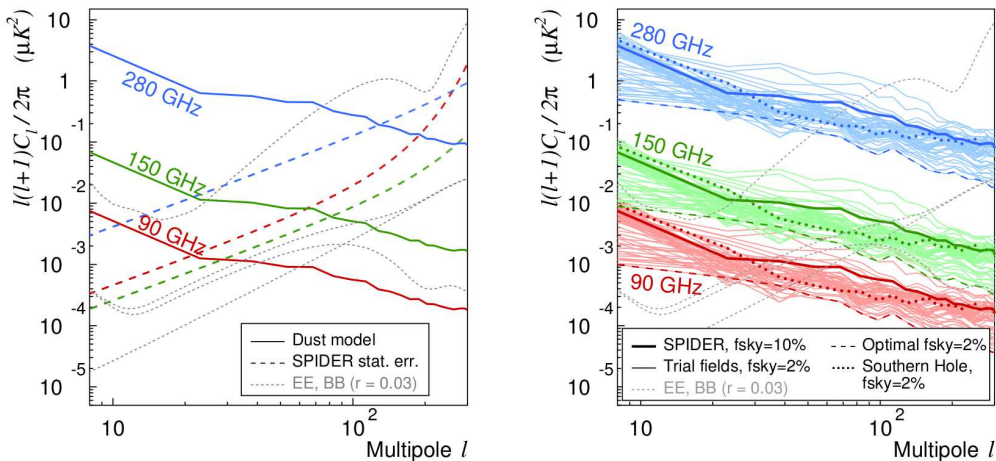
Figure 3 *Left:* A multipole-by-multipole comparison of the levels of statistical noise at each frequency in Table 1 after both flights and of the astrophysical and cosmological signals, including Galactic foregrounds, lensing, and the B-mode signal assuming a scalar-to-tensor ratio $r = 0.03$. *Right:* Level of Galactic foreground emission in the nominal SPIDER field ($f_{sky} = 10\%$) compared to constituent trial fields with $f_{sky} = 2\%$. The optimal 2% of the sky, outlined in Figure 4, has the lowest polarized dust emission at $50 < \ell < 200$ not only within the SPIDER region, but also within the entire area of sky accessible from a McMurdo LDB flight. Spectra are also shown for a trial field centered on ($\alpha = 0°$, $\delta = -57°$), which lies within the "Southern Hole," a target region used by several ground-based experiments. Note that our foreground model does not include polarized synchrotron emission from the Galaxy given the weakness of this signal in our bands in the SPIDER region (see discussion in Section 3.1).

The left panel of Figure 3 shows the power spectra of the polarized Galactic dust emission in the SPIDER field for all three frequencies in Table 1, along with the per-multipole statistical error for each band after both flights as predicted by a Fisher analysis (see Section 5). At a given frequency, the brightness of the polarized emission from interstellar dust in the SPIDER field is comparable to that of the full-sky average of this signal (Galactic plane excluded), whose characteristics were described in Section 3.1. Interestingly, it is also comparable to that of the polarized Galactic dust emission in a typical $f_{sky} = 2\%$ patch in the popular "Southern Hole" region, as shown in the right panel of Figure 3, even though SPIDER will observe five times as much sky as covered by this patch. This appears to indicate that although the Southern Hole is believed to be the region of the southern sky most free of dust emission, it might not be the region most free of *polarized* dust emission. Finally, it is worth noting that the SPIDER region encompasses the cleanest 2% of the sky accessible from a McMurdo LDB flight, and that a large majority of its component fields exhibit significantly less polarized Galactic dust emission than the region average (the relevant power spectra are also shown in the right panel of Figure 3). This will provide valuable cross-checks to evaluate the level of foreground contamination in the SPIDER maps.

Table 3.

Summary of general information on the SPIDER mission	
Launch Location	McMurdo Station, Antarctica
Launch Date	12/2013 (Flight 1), 12/2015 (Flight 2)
Flight Duration (target)	20 days per flight
Altitude (target)	36,000 m
Flight Path	Circumpolar, typically $73°S <$ latitude $< 82°S$
Sky Coverage	$f_{sky} \sim 0.1$, $10 \lesssim \ell \lesssim 300$

Note. — The flight schedule provided in this table is consistent with the state of hardware development as of August 2012.
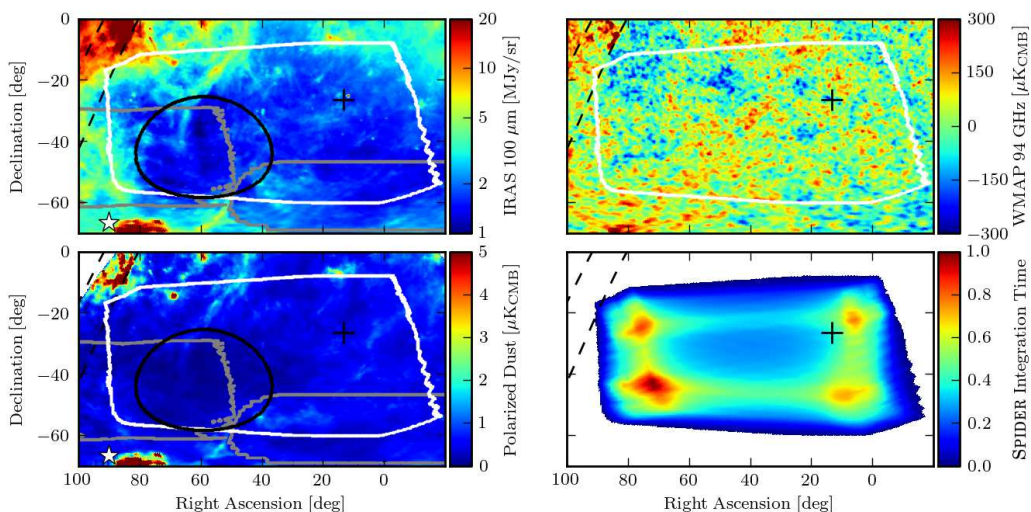
Figure 4 SPIDER observing region and scan profile. All four panels show the same portion of the sky, in equatorial coordinates, smoothed with a 30' beam. The southern Galactic pole (black +) is overplotted, along with the 10- and 20-degree Galactic latitude lines (dashed). *Top left:* IRAS 100 μm data showing dust morphology, the SPIDER observing region (white outline), and the south ecliptic pole (white $\star$). Also shown are the BOOMERANG and BICEP fields (left and right gray outlines, respectively), and the region of minimum foreground contamination in the SPIDER field (black outline). *Bottom left:* Polarized dust emission amplitude at 150 GHz, according to the model in Section 3.2. Clear differences in dust emission morphology are visible between this model and the IRAS data. *Top right:* WMAP 94 GHz *TT* data in the same area, showing relative absence of foreground contamination in the SPIDER observation region. *Bottom right:* Distribution of integration time, averaged over all detectors in a single 150 GHz focal plane, for the observing strategy in Section 4.1.

4 Observing strategy

4.1 Overview

SPIDER will launch its first flight from McMurdo Station in Antarctica in December 2013, and observe the southern sky for about 20 days. The flight parameters are summarized in

Table 3. The observing strategy is designed to maximize sky coverage and crosslinking over the cleanest regions of the sky accessible from a McMurdo LDB flight. Figure 4 shows the intensity and polarization of the Galactic dust emission in the SPIDER region [33], as well as the relatively foreground-free CMB sky in the 94 GHz *WMAP* band.

The baseline scan strategy consists of azimuthal scans punctuated by elevation steps and rotations of the half-wave plate. The scan velocity profile is sinusoidal with a maximum acceleration of 0.8 degrees/s² (for a scan period of ∼45 seconds). The exact scan amplitude and center is adapted at each elevation step to (i) avoid observing within 90 degrees of the Sun, as set by the design of the sun shield, and (ii) maintain the instrument boresight pointing at the region of the southern sky outside of the Galactic plane (0 to 80 degrees right ascension). Elevation steps occur every hour, in sync with local sidereal time (LST). We reach maximum elevation (40 degrees) at 12:00 LST, and minimum elevation (28 degrees) at 24:00 LST. By syncing the elevation steps with sidereal time, we ensure maximal sky coverage in declination. The sky coverage repeats each sidereal day, providing both redundancy and a rich set of consistency tests. Once per day, when sky rotation is at a minimum at local midnight or noon (depending on when observations begin), we rotate the half-wave plate of each instrument by 22.5°, thereby switching Q to U in the instrument frame.

We set aside time after each half-wave plate rotation to perform beam and pointing calibrations on Galactic sources. Every half hour, near the beginning and end of each constant-elevation period, we perform a brief (∼5 s) in-flight measurement of detector responsivity by slightly stepping the detector biases. Each sub-Kelvin cooler must be re-cycled every 72 hours. To reduce the instantaneous load on the 1.6 K stage, these cycles must be staggered. The cycling of one instrument has no impact on the others, allowing for a ∼85% observational duty cycle. The process of cycling all six coolers requires four hours for all instruments to return to the nominal base temperature.

We estimate the effect that the observing profile will have on the Stokes $T/Q/U$ reconstruction, assuming an ideal case of no beam asymmetry, no $T \to Q, U$ leakage (i.e. perfect polarization efficiency), and no noise correlation between detectors. We calculate the pointing matrix A_p for each pixel p, as

$$A_p = \left\langle \begin{bmatrix} 1 & \cos 2\psi & \sin 2\psi \\ \cos 2\psi & \cos^2 2\psi & \cos 2\psi \sin 2\psi \\ \sin 2\psi & \cos 2\psi \sin 2\psi & \sin^2 2\psi \end{bmatrix} \right\rangle_p, \qquad (4.1)$$

where $\langle \ldots \rangle_p$ indicates the average over all $i = 1 \ldots N_{\mathrm{obs},p}$ observations along p at the series of polarization angles $\{\psi_{p,i}\}$. The inverse of A_p gives an estimate of the signal $T/Q/U$ covariance for each pixel. In the ideal case, we would have $A_p^{-1} = \mathrm{diag}(1, 2, 2)$. We therefore construct a figure of merit, which we call the "fractional excess variance in polarization," from the QQ and UU elements of A_p^{-1}:

$$F_p = \frac{1}{2} \left[\sqrt{(A_p^{-1})_{QQ}} - \sqrt{2} \right]^2$$
$$+ \frac{1}{2} \left[\sqrt{(A_p^{-1})_{UU}} - \sqrt{2} \right]^2. \qquad (4.2)$$

This figure of merit is shown in Figure 5, for a single detector, and for a full focal plane of 256 pixels (2 detectors per pixel). The excess variance is below 1% over 96% of the observed region. We will fly with pairs of telescopes clocked at 45° relative to each other, which allows a
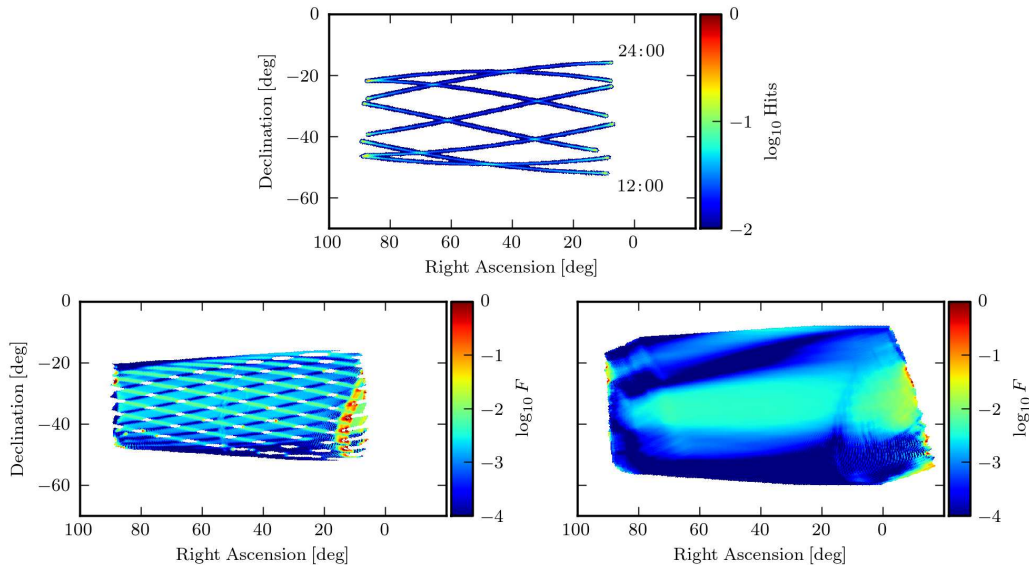
Figure 5 The SPIDER scan profile. All three panels show the same portion of the southern sky, in equatorial coordinates, smoothed with a 30' beam. *Top:* A 24-hour period for a single detector, illustrating the change in telescope orientation throughout the day. Five-minute periods every three hours are shown. Detector pairs in a single pixel are oriented 22.5 and 112.5 degrees relative to the scan direction. *Bottom left:* Fraction of excess variance (see definition in Section 4.1) due to anisotropic angular coverage in the Stokes Q and U maps for the above detector over a four-day period. *Bottom right:* Fraction of excess variance for a full focal plane of 512 bolometers, over a four-day period. This observing profile covers 9.5% of the sky, of which 96% is observed with near-isotropic coverage in crossing angles to reconstruct the Stokes Q and U parameters with $< 1\%$ excess variance.

simultaneous measurement of both Q and U parameters, significantly improving crosslinking in the maps and further reducing the excess variance.

4.2 Filter transfer function F_ℓ

The interplay between scan strategy and instrumental and environmental effects plays a significant role in all CMB experiments. These instrumental effects include scan-synchronous artifacts, ground-fixed signals, atmospheric contamination, and low-frequency instability in the instrument. Signal estimation pipelines tend to be tailored to each experiment (or flight of the same experiment) according to the particular combination of effects that are most relevant to each dataset.

While these algorithms, which include template removal, common mode decorrelation, and (statistical) least-squares mapmaking, are generally quite effective at removing systematic effects from the data, they nevertheless result in a degradation of sensitivity and the loss of fidelity to particular spatial modes of the astrophysical signal relative to an idealized dataset consisting only of the signal and Gaussian uncorrelated white noise. SPIDER is no exception, and we study the impact of these effects through time domain simulations of the experiment that capture as fully as possible the range of instrumental and environmental effects that are present in the data.

The impact on the fidelity of the recovered CMB power spectrum can be approximately characterized via a calculation of the transfer function F_ℓ, as determined by the comparison of a modest ensemble of signal simulations to the input sky [51]. An understanding of this transfer function is necessary to relate NET estimates of any experiment, for example those in Table 1, to errors on CMB power spectra or experimental upper limits. As we will show, the relatively benign stratospheric balloon environment coupled with SPIDER's large sky coverage provide polarized maps of the sky with extremely low noise and high fidelity to angular scales ranging from the scale of the map to that of the beam.

For SPIDER, we expect the large angular scales to be dominated by noise at time scales below the half-period of an azimuthal scan, which varies between ~ 20–25 s, depending on the scan amplitude. Contributions to the noise include a scan synchronous component from the residual atmospheric column as well as $1/f$ noise from instability on the bias and instrumental backgrounds. While the stationary Gaussian component of the noise can be optimally accounted for by the use of a least-squares mapmaker [see, e.g., 52], we expect, based on our experience with past balloon experiments, the need to apply additional filtering to remove a scan-synchronous component and reduce the impact of uncertainty in the low-frequency transfer function.

We measure the net effect of signal processing on the power spectrum by calculating the transfer function F_ℓ following the formalism developed in [51]. We calculate the power spectrum $\hat{C}_\ell^{(\mathrm{in})}$ of a signal-only CMB realization that has been smoothed by the beam (30′ FWHM for the 150 GHz instrument). We then apply the observing profile shown in Figures 4 and 5 to generate noise-free time-ordered data for processing. These simulated data are then input to the signal estimation pipeline, which incorporates our estimate of the noise spectra, flagging and any additional filtering. We then calculate the power spectrum $\hat{C}_\ell^{(\mathrm{out})}$ of the resultant maps. Both the input and output maps are weighted by the distribution of integration time shown in Figure 4 to ensure identical cut-sky treatment. The transfer function is then simply the ratio of the input and output power spectra, averaged over an ensemble of realizations.

Figure 6 shows the published transfer functions for BICEP and BOOMERANG03, as well as two estimates for SPIDER that correspond to optimistic and pessimistic levels of scan-synchronous noise. Results are shown for the temperature anisotropy power spectrum only; measurements of the polarized filter function are ongoing, but are not qualitatively different. We multiply the transfer function with the beam to illustrate the combined effect on the power spectrum. At large angular scales, we lose modes due to interplay between the filtering and the scan, while small angular scales are downweighted by the beam. The relatively severe required filtering applied in BICEP reduces the product of the transfer function and beam window function to nearly 50% at the peak. In the optimistic scenario for SPIDER, we set the high-pass filter cutoff just above the azimuthal scan frequency (25 mHz), which leads to the peak nearing 90% at $\ell \sim 50$ even with a naively binned map. More realistically, we have set the cutoff near 50 mHz, corresponding to a half-period of the scan. This choice is informed by the data from BOOMERANG, and corresponds to the most stringent filtering that had to be applied to the polarization data from the 2003 flight (towards the end of the flight, at the relatively low altitude of ~ 30 km). SPIDER preserves fidelity to larger scales (lower multipoles) than BOOMERANG simply because of the larger sky coverage and higher scan rate, and not because the SPIDER data are expected to be qualitatively more stable or well behaved than the BOOMERANG data. While this more aggressive filtering reduces the transfer function at $\ell \sim 10$ by over 50%, the peak at $\ell \sim 70$ remains relatively high at 85%.
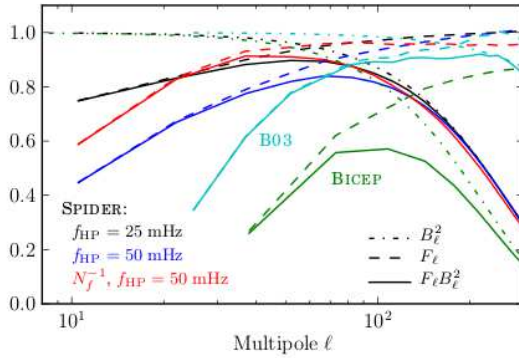
Figure 6 An estimate of the filter transfer function F_ℓ^{TT} and beam function B_ℓ for SPIDER's 150 GHz instrument, shown alongside transfer functions for typical ground-based [BICEP, 11] and balloon-borne [BOOMERANG03, 53] experiments. The transfer function for SPIDER is estimated from an ensemble of signal realizations assuming time-domain filtering of signals below the azimuthal scan frequency. The black and blue curves were calculated from high-pass filtered signals naively binned into maps, while the red curve was obtained using an iterative least-squares mapmaker that took into account both a high-pass filter and the expected bolometer noise PSD. The low-frequency noise is well approximated by a power-law with a spectral index of -0.75 and a knee at 0.15 Hz.

The covariance of the band power estimates derived from the data depends on the effect of the experiment on both sample and statistical variance. The sample error on the measured power spectrum $\hat{C}_\ell$ increases as $1/\sqrt{F_\ell}$ as the effective number of observed modes is reduced. While this increase in the sample variance has no impact on the ability of an experiment to set upper limits on the B-mode spectrum, the impact of the processing on the statistical variance does.

To account for detector noise, we use an iterative least-squares mapmaker similar to that in [52] on the filtered data. The inverse-noise kernel is estimated from a typical noise power spectrum, measured in our system with no optical loading on the bolometers. The absence of (Gaussian and white) photon noise in this measurement provides an accurate estimate of the instrumental noise. The significant features in the noise power spectrum are (1) a $1/f$ knee at ~ 100 mHz, and (2) excess noise at frequencies above ~ 10 Hz, likely due to the thermal architecture of the bolometer island, which reduces the asymptotic transfer function by $\sim 5\%$. The iterative method improves the net transfer function by up to 30% relative to the naively binned case at the largest scales. Recent bolometer noise measurements under optical loading with improved bias stability show that the $1/f$ knee is likely to be closer to 25 mHz in flight, which should further improve the large-scale transfer function.

5   Band selection & prospects for foreground removal

In this section, we evaluate the ability of SPIDER to detect inflationary B-modes as a function of the frequency distribution of FPU·flights (number of focal plane units multiplied by number of flights). In addition to the 90 GHz, 150 GHz, and 280 GHz channels whose characteristics are given in Table 1, we consider the possibility of adding a 220 GHz frequency band. This frequency was chosen to be half way between SPIDER's 150 GHz and 280 GHz channels, thereby eliminating the frequency coverage gap that results from the frequency distribution

in Table 1. The 220 GHz band would have the same number of detectors per FPU as the 280 GHz band. Its bandwidth and its beam's FWHM would be 53 GHz and 21′, respectively. The sensitivity of each of its detectors would be 320 μK$_{\mathrm{CMB}}\sqrt{\mathrm{s}}$, for an overall FPU sensitivity of 15 μK$_{\mathrm{CMB}}\sqrt{\mathrm{s}}$. For programmatic reasons, we require that observations at each frequency during each flight be performed by at least two FPUs. For each SPIDER flight, we therefore have the option to acquire data at up to three frequencies to be chosen among 90 GHz, 150 GHz, 220 GHz, and 280 GHz. Since, as discussed in Section 3, the emission from Galactic dust is expected to become stronger with increasing frequency, Galactic foregrounds are expected to be lower at 90 and 150 GHz than at 220 and 280 GHz. As a result, we choose 90 GHz and 150 GHz as two of the three SPIDER bands for the first flight, and perform numerical simulations to distribute the remaining two FPUs.

We simulate a hundred maps at each frequency with independent CMB and noise realizations. CMB maps are obtained with *WMAP*'s best fit ΛCDM cosmological parameters, $r = 0.03$, and CMB lensing included. We approximate the noise in SPIDER as white, governed by the parameters in Table 1 (for the 220 GHz band, we use the parameters listed in the previous paragraph), and weighted by the expected number of observations per pixel for the observing strategy in Section 4.1. Each simulated map is added to a template for the Galactic dust emission at the appropriate wavelength. Dust templates are extrapolated from the 90 GHz map from [33] described in Section 3 assuming a single power-law dependence on frequency with spectral index $\beta_{\mathrm{d}} = 1.7$, the latter being the average of the one-index best fit to the Finkbeiner-Davis-Schlegel (FDS) model 8 [41] and of *WMAP*'s "base" fit dust spectral index [54]. Note that we do not attempt to use a two-component dust model. In some of the cases we consider in this section, this would indeed lead to more parameters than we can possibly fit given the number of observing bands in play.

With two pairs of FPUs occupied by either 90 GHz or 150 GHz detectors, we use a simple pixel-by-pixel least-square foreground fitting procedure to evaluate SPIDER's first flight's ability to detect *B*-modes when the two remaining FPUs are assigned to (i) 90 GHz and 150 GHz, (ii) 220 GHz, or (iii) 280 GHz. In order to have similar signal-to-noise ratios at the two low-foreground frequencies, we do not consider cases in which the numbers of FPUs at 90 and 150 GHz differ. We model the data as

$$\mathbf{S} = \mathbf{S}_{\mathrm{CMB}} + \mathbf{S}_{\mathrm{d},\nu_0} \left(\frac{\nu}{\nu_0} \right)^{\beta_{\mathrm{d}}}, \tag{5.1}$$

where $\mathbf{S}$ is the usual set of Stokes parameters, the index d refers to dust, and $\nu_0 = 90$ GHz, and fit the seven free parameters to the simulated data. In all cases, we include as part of the data a *Planck* 217 GHz map simulated in the same way as the SPIDER maps with the instrument characteristics published in the *Planck* early papers [20].

Given SPIDER's focus on characterizing the $\ell \sim 80$ *B*-mode peak, we use the $\ell = 80$ *B*-mode signal-to-noise ratio (SNR) computed from residual maps as a figure of merit to assess the quality of the CMB reconstruction. Among the three cases we consider for the first SPIDER flight, having three FPUs at 90 GHz and three FPUs at 150 GHz leads to the highest *B*-mode SNR at $\ell = 80$, and therefore to the best reconstructed CMB map for our purposes. This configuration turns out to be also favored from a detector development point of view.

After the first SPIDER flight, we expect the per-multipole statistical error at 150 GHz to be at a level comparable to that of the power spectrum of our foreground model at $\ell \sim 80$. With Galactic dust now limiting our ability to detect inflationary *B*-modes, we

Table 4. SPIDER FPU frequency distribution and per-band cumulative noise

| Flight	FPU Distribution	Cumulative Noise (μK$_{\mathrm{CMB}}$/deg^2)		
		90 GHz	150 GHz	280 GHz
SPIDER 1	3×90 GHz; 3×150 GHz	0.27	0.20	$\cdots$
SPIDER 2	2×90 GHz; 2×150 GHz; 2×280 GHz	0.21	0.16	0.62

Note. — The multiple telescopes at each frequency are rotated with respect to one another to simultaneously recover Q and U in each daily map. The distribution of observing frequencies is chosen following the procedure described in Section 5 so as to maximize SPIDER's ability to detect inflationary B-modes at angular scales corresponding to $\ell \sim 80$. The cumulative noise numbers use the parameters listed in Table 1.
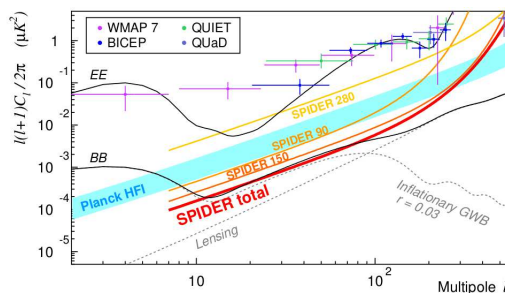
Figure 7 Theoretical E-mode and B-mode (EE and BB) power spectra and projected per-multipole statistical errors for SPIDER after both flights and for *Planck* HFI. E-mode detections from *WMAP* [55], BICEP [11], QUIET [12], and QUaD [6] are also shown for comparison. The B-mode spectrum is the sum of two components (dotted lines): inflationary gravitational waves, shown here for $r = 0.03$, and weak gravitational lensing of E-mode polarization. The noise curves for SPIDER and *Planck* are derived from a simple Fisher analysis, assuming no foreground contamination. It is likely that foreground emission will limit *Planck*'s measurement of the BB bump below $\ell \simeq 10$ (corresponding to an angular scale of $\gtrsim 20$ degrees) induced by reionization. SPIDER is optimized to cover the $\ell \sim 80$ peak in the gravitational wave spectrum. The SPIDER band powers have been truncated at a multipole of seven as the limited sky coverage will prevent us from probing larger scales.

seek to increase SPIDER's frequency coverage in order to gather multi-frequency foreground information, which will help constrain the model in Equation (5.1). Given the programmatic constraints previously mentioned and continued observations at 90 GHz and 150 GHz, this can be achieved only by flying a pair of either 220 GHz or 280 GHz FPUs. Performing an analysis similar to that described above for the first SPIDER flight, we select the 280 GHz band over the 220 GHz channel, which leads to the FPU·flight distribution listed in Table 4 along with the cumulative noise in each band. Figure 7 shows the resulting per-multipole statistical error in each band after both flights, as well as the overall statistical error for the full mission, both derived from a Fisher analysis. The expected *Planck* HFI statistical error from a similar analysis is also shown for comparison.

Figure 8 shows forecasts for the constraints on the tensor-to-scalar ratio r from SPIDER (after one and both flights) and from *Planck*. These constraints are derived using the method
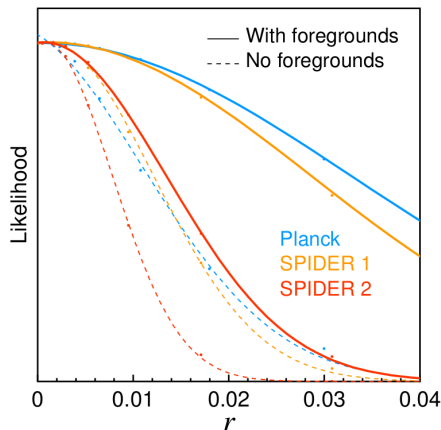
Figure 8 Marginalized one-dimensional r-likelihood curves for SPIDER and *Planck* HFI. In the "with foreground" case, foreground-subtraction residuals are included as contaminants. The "no foreground" case assumes no foreground contamination. In the absence of foregrounds, the first flight of SPIDER (SPIDER 1) achieves the 3σ limit $r < 0.03$, while the two flights combined (SPIDER 2) lead to $r < 0.02$ (99% CL). In the "with foreground" case, two flights are needed to reach the 3σ limit $r < 0.03$. The details of the two flights are given in Table 4.

described in detail in Farhang et al. (submitted), which we summarize below.

Assuming a uniform *a priori* probability distribution for the cosmological parameters $\mathbf{q}$, the *a posteriori* distribution function's dependence on $\mathbf{q}$ is given by the likelihood $\mathcal{L}_{\boldsymbol{\Delta}}(\mathbf{q}) \equiv P(\boldsymbol{\Delta}|\mathbf{q})$, the probability of the data $\boldsymbol{\Delta}$ given the parameters, such that

$$- 2 \ln \mathcal{L}_{\boldsymbol{\Delta}}(\mathbf{q}) = \boldsymbol{\Delta}^\dagger \, \mathbf{C}_{\text{tot}}^{-1} \, \boldsymbol{\Delta} + \ln |(2\pi)^{N_{\text{pix}}} \, \mathbf{C}_{\text{tot}}|, \tag{5.2}$$

where $\boldsymbol{\Delta}$ is the full set of CMB temperature and polarization maps including both signal and noise, N_{pix} is the number of pixels in the maps, and $\mathbf{C}_{\text{tot}} \equiv \mathbf{C}_{\text{N}} + \mathbf{C}_T(\mathbf{q})$ is the theoretical pixel-pixel covariance matrix with contributions from both the parameter-dependent signal covariance $\mathbf{C}_T(\mathbf{q})$ and the generalized noise covariance $\mathbf{C}_{\text{N}}$. The latter includes uncertainties from foreground subtraction as well as from noise in the maps.

Here, we calculate the likelihood in Equation (5.2) on a two-dimensional grid consisting of the cosmological parameters r and τ, the latter referring to the Thomson scattering optical depth to reionization. Although extra dimensions could be added, Farhang et al. (submitted) show that r is only weakly correlated with other standard cosmological parameters in the small-r, small-f_{sky} limit of relevance to SPIDER. Since stringent constraints on τ are an objective of large-scale experiments such as *Planck*, we marginalize over it in order to evaluate whether insensitivity to it will impact SPIDER's ability to constrain r. It appears that with our sky coverage fixed at 10%, r and τ are essentially uncorrelated.

The results in Figure 8 assume $f_{\text{sky}} = 0.75$ for *Planck* and $f_{\text{sky}} = 0.10$ for SPIDER, and are given for two cases: "with" and "without" foregrounds. In the former case, foreground residuals after the removal procedure described earlier in this section are included as contaminants, whereas in the latter case, it is assumed that there is no foreground contamination in the maps. Since we seek to derive the most stringent upper limit on r that SPIDER could set given the assumptions in this paper, the input cosmological model assumes $r = 0.001$ (and

$\tau = 0.09$). Farhang et al. (submitted) address the question of how well "large"-r B-modes can be detected.

We find that, with two flights, SPIDER has the ability to constrain the value of the tensor-to-scalar ratio r to below 0.03 (99% CL). This number improves to 0.02 (99% CL) in the limit of no foreground contamination. It is worth noting that the constraint quoted above for the "with foreground" case is based on the foreground removal technique described earlier in this section, which assumes that the frequency dependence of the polarized dust emission is well described by a single power law. Although this is in line with the current state-of-the-art for B-mode forecasts [see, e.g., 39], the detailed question of how deviations from this description will be handled has yet to be studied. Any such deviation will likely impact the quoted constraints [see, e.g., 56]. Relatedly, it is possible that a different frequency dependence of the polarized dust emission might require a different frequency coverage in order to reach the best possible constraints on r. Should this become apparent after the first SPIDER flight, or through improvements in our knowledge of foregrounds before SPIDER flies, the flexibility of SPIDER's focal plane composition discussed in Section 2.1 ensures that we will be able to adopt the best frequency coverage to reach our science goals.

6 Summary & conclusions

Our main results are as follows.

1. The SPIDER instrument was designed with an emphasis on reaching low levels of polarized systematic error at multipoles close to the $\ell \sim 80$ acoustic peak in the B-mode power spectrum (Section 2.1). Taking into account all known sources of systematic error, the residual power spectrum is less than 37% of the B-mode signal for $r = 0.03$ at $\ell = 100$ (Section 2.2). As we refine our systematics budget, we expect this number to go down for three reasons: (1) more stringent design targets than those shown in Table 2 have already been reached; (2) recent updates to our flight plan and to our scanning strategy are expected to reduce the overall level of systematic error by providing better observing conditions; and (3) all residuals in Table 2 were added in quadrature, which leads to a conservative estimate of the global systematic error. Simulations taking these three points into account are underway. The reduction in systematic error that we expect these improved simulations to show will likely be partially canceled by the inclusion of systematic effects that are yet to be characterized, in particular in so far as they relate to thermal stability of the focal plane and of the optical sleeve.

2. Polarized sidelobes should not hinder SPIDER's ability to detect or constrain B-modes. Using the polarized sidelobe profile measured in BICEP, we showed that the corresponding contamination at $\ell = 100$ is over an order of magnitude fainter than the $r = 0.03$ B-mode signal (Section 2.3). As illustrated in Figure 2, improved baffling will lower this number by over an order of magnitude. At the largest scales ($\ell \sim 10$), it will lead to a polarized sidelobe signal of amplitude comparable to that of the $r = 0.03$ B-modes.

3. SPIDER's observing strategy (Section 4.1) was designed to minimize the $T/Q/U$ covariance, thereby minimizing the uncertainty in the reconstruction of the Stokes parameters. Figure 5 shows that, taking all detectors into account, the excess variance introduced by the scanning strategy is less than 1% over 96% of the sky observed during a 4-day period.

4. The lack of atmospheric contamination at stratospheric altitude and large sky coverage enabled by SPIDER's small apertures provide a relatively broad dynamic range in multipole, as shown by the filter transfer function (F_ℓ) study in Section 4.2. This opens the possibility of moving beyond detection to a spectral characterization of the B-mode power spectrum, an important consistency check on the cosmological origin of any detected signal. Furthermore, the fidelity of the measurement results in a significantly higher final sensitivity than would be achieved by an experiment of the same NET using a less efficient observation platform.

5. The frequency distribution as a function of SPIDER flight summarized in Table 4 ensures high signal-to-noise measurements of the microwave sky at low-foreground frequencies, while the polarized emission from interstellar dust is mapped with high sensitivity in a band where it overwhelmingly dominates. With this distribution, we showed in Section 5 that SPIDER will provide the stringent constraint $r < 0.03$ (99% CL) after both flights, even when accounting for residual foreground contamination. This number is derived under the assumption that the *Planck* 217 GHz data will be available during the SPIDER analysis. When foreground contamination is ignored, SPIDER's constraint improves to $r < 0.02$ (99% CL).

6. Among Galactic foregrounds, we expect the polarized emission from interstellar dust to be the only signal as bright or brighter than the $r = 0.03$ B-modes at SPIDER frequencies (Section 3.1). We model this emission following the procedure detailed in Section 3.2, and show that the SPIDER observing region includes the cleanest 2% of the sky accessible from a McMurdo LDB flight. The average amplitude of the polarized Galactic dust emission in the SPIDER field is comparable to that in a typical $f_{\rm sky} = 2\%$ patch in the "Southern Hole;" many $f_{\rm sky} = 2\%$ patches in the SPIDER region exhibit significantly less polarized dust emission. This study suggests that without component separation, degree-scale polarized dust emission will limit the constraints of *any* experiment at or above the level of $r \sim 0.03$, *even in the portions of the southern sky most free of Galactic dust emission.*

Although more work is needed to fully characterize the SPIDER instrument and its nontrivial interaction with the microwave sky, a simple Galactic foreground situation could allow SPIDER to characterize a cosmological B-mode signal whose intensity is close to the lowest compatible with the simplest viable class of inflationary models. General studies of the impact of a more complex foreground situation have yet to be performed, and are of obvious interest in the context of SPIDER.

Acknowledgments

---

[1]http://healpix.jpl.nasa.gov

subroutine library [58]. This research has made use of NASA's Astrophysics Data System. We acknowledge the use of the Legacy Archive for Microwave Background Data Analysis (LAMBDA). Support for LAMBDA is provided by the NASA Office of Space Science.

References

[1] G. F. Smoot, C. L. Bennett, A. Kogut, E. L. Wright, J. Aymon, N. W. Boggess, E. S. Cheng, G. de Amici, S. Gulkis, M. G. Hauser, G. Hinshaw, P. D. Jackson, M. Janssen, E. Kaita, T. Kelsall, P. Keegstra, C. Lineweaver, K. Loewenstein, P. Lubin, J. Mather, S. S. Meyer, S. H. Moseley, T. Murdock, L. Rokke, R. F. Silverberg, L. Tenorio, R. Weiss, and D. T. Wilkinson, *Structure in the COBE differential microwave radiometer first-year maps*, Astroph. J. Lett. **396** (Sept., 1992) L1–L5.

[2] P. de Bernardis, P. A. R. Ade, J. J. Bock, J. R. Bond, J. Borrill, A. Boscaleri, K. Coble, B. P. Crill, G. De Gasperis, P. C. Farese, P. G. Ferreira, K. Ganga, M. Giacometti, E. Hivon, V. V. Hristov, A. Iacoangeli, A. H. Jaffe, A. E. Lange, L. Martinis, S. Masi, P. V. Mason, P. D. Mauskopf, A. Melchiorri, L. Miglio, T. Montroy, C. B. Netterfield, E. Pascale, F. Piacentini, D. Pogosyan, S. Prunet, S. Rao, G. Romeo, J. E. Ruhl, F. Scaramuzzi, D. Sforna, and N. Vittorio, *A flat Universe from high-resolution maps of the cosmic microwave background radiation*, Nature **404** (Apr., 2000) 955–959.

[3] D. N. Spergel, L. Verde, H. V. Peiris, E. Komatsu, M. R. Nolta, C. L. Bennett, M. Halpern, G. Hinshaw, N. Jarosik, A. Kogut, M. Limon, S. S. Meyer, L. Page, G. S. Tucker, J. L. Weiland, E. Wollack, and E. L. Wright, *First-Year Wilkinson Microwave Anisotropy Probe (WMAP) Observations: Determination of Cosmological Parameters*, Astroph. J. Suppl. **148** (Sept., 2003) 175–194.

[4] L. Page, G. Hinshaw, E. Komatsu, M. R. Nolta, D. N. Spergel, C. L. Bennett, C. Barnes, R. Bean, O. Doré, J. Dunkley, M. Halpern, R. S. Hill, N. Jarosik, A. Kogut, M. Limon, S. S. Meyer, N. Odegard, H. V. Peiris, G. S. Tucker, L. Verde, J. L. Weiland, E. Wollack, and E. L. Wright, *Three-Year Wilkinson Microwave Anisotropy Probe (WMAP) Observations: Polarization Analysis*, Astroph. J. Suppl. **170** (June, 2007) 335–376.

[5] J. M. Kovac, E. M. Leitch, C. Pryke, J. E. Carlstrom, N. W. Halverson, and W. L. Holzapfel, *Detection of polarization in the cosmic microwave background using DASI*, Nature **420** (Dec., 2002) 772–787.

[6] M. L. Brown, P. Ade, J. Bock, M. Bowden, G. Cahill, P. G. Castro, S. Church, T. Culverhouse, R. B. Friedman, K. Ganga, W. K. Gear, S. Gupta, J. Hinderks, J. Kovac, A. E. Lange, E. Leitch, S. J. Melhuish, Y. Memari, J. A. Murphy, A. Orlando, C. O'Sullivan, L. Piccirillo, C. Pryke, N. Rajguru, B. Rusholme, R. Schwarz, A. N. Taylor, K. L. Thompson, A. H. Turner, E. Y. S. Wu, M. Zemcov, and The QUaD collaboration, *Improved Measurements of the Temperature and Polarization of the Cosmic Microwave Background from QUaD*, Astroph. J. **705** (Nov., 2009) 978–999.

[7] C. L. Reichardt, P. A. R. Ade, J. J. Bock, J. R. Bond, J. A. Brevik, C. R. Contaldi, M. D. Daub, J. T. Dempsey, J. H. Goldstein, W. L. Holzapfel, C. L. Kuo, A. E. Lange, M. Lueker, M. Newcomb, J. B. Peterson, J. Ruhl, M. C. Runyan, and Z. Staniszewski, *High-Resolution CMB Power Spectrum from the Complete ACBAR Data Set*, Astroph. J. **694** (Apr., 2009) 1200–1219.

[8] E. Komatsu, K. M. Smith, J. Dunkley, C. L. Bennett, B. Gold, G. Hinshaw, N. Jarosik, D. Larson, M. R. Nolta, L. Page, D. N. Spergel, M. Halpern, R. S. Hill, A. Kogut, M. Limon, S. S. Meyer, N. Odegard, G. S. Tucker, J. L. Weiland, E. Wollack, and E. L. Wright, *Seven-year Wilkinson Microwave Anisotropy Probe (WMAP) Observations: Cosmological Interpretation*, Astroph. J. Suppl. **192** (Feb., 2011) 18–+.

[9] S. Das, T. A. Marriage, P. A. R. Ade, P. Aguirre, M. Amiri, J. W. Appel, L. F. Barrientos, E. S. Battistelli, J. R. Bond, B. Brown, B. Burger, J. Chervenak, M. J. Devlin, S. R. Dicker, W. Bertrand Doriese, J. Dunkley, R. Dünner, T. Essinger-Hileman, R. P. Fisher, J. W. Fowler, A. Hajian, M. Halpern, M. Hasselfield, C. Hernández-Monteagudo, G. C. Hilton, M. Hilton, A. D. Hincks, R. Hlozek, K. M. Huffenberger, D. H. Hughes, J. P. Hughes, L. Infante, K. D. Irwin, J. Baptiste Juin, M. Kaul, J. Klein, A. Kosowsky, J. M. Lau, M. Limon, Y.-T. Lin, R. H. Lupton, D. Marsden, K. Martocci, P. Mauskopf, F. Menanteau, K. Moodley, H. Moseley, C. B. Netterfield, M. D. Niemack, M. R. Nolta, L. A. Page, L. Parker, B. Partridge, B. Reid, N. Sehgal, B. D. Sherwin, J. Sievers, D. N. Spergel, S. T. Staggs, D. S. Swetz, E. R. Switzer, R. Thornton, H. Trac, C. Tucker, R. Warne, E. Wollack, and Y. Zhao, *The Atacama Cosmology Telescope: A Measurement of the Cosmic Microwave Background Power Spectrum at 148 and 218 GHz from the 2008 Southern Survey*, *Astroph. J.* **729** (Mar., 2011) 62–+.

[10] R. Keisler, C. L. Reichardt, K. A. Aird, B. A. Benson, L. E. Bleem, J. E. Carlstrom, C. L. Chang, H. M. Cho, T. M. Crawford, A. T. Crites, T. de Haan, M. A. Dobbs, J. Dudley, E. M. George, N. W. Halverson, G. P. Holder, W. L. Holzapfel, S. Hoover, Z. Hou, J. D. Hrubes, M. Joy, L. Knox, A. T. Lee, E. M. Leitch, M. Lueker, D. Luong-Van, J. J. McMahon, J. Mehl, S. S. Meyer, M. Millea, J. J. Mohr, T. E. Montroy, T. Natoli, S. Padin, T. Plagge, C. Pryke, J. E. Ruhl, K. K. Schaffer, L. Shaw, E. Shirokoff, H. G. Spieler, Z. Staniszewski, A. A. Stark, K. Story, A. van Engelen, K. Vanderlinde, J. D. Vieira, R. Williamson, and O. Zahn, *A Measurement of the Damping Tail of the Cosmic Microwave Background Power Spectrum with the South Pole Telescope*, *ArXiv e-prints* (May, 2011) [`arXiv:1105.3182`].

[11] H. C. Chiang, P. A. R. Ade, D. Barkats, J. O. Battle, E. M. Bierman, J. J. Bock, C. D. Dowell, L. Duband, E. F. Hivon, W. L. Holzapfel, V. V. Hristov, W. C. Jones, B. G. Keating, J. M. Kovac, C. L. Kuo, A. E. Lange, E. M. Leitch, P. V. Mason, T. Matsumura, H. T. Nguyen, N. Ponthieu, C. Pryke, S. Richter, and K. W. Yoon, *Measurement of Cosmic Microwave Background Polarization Power Spectra from Two Years of BICEP Data*, *Astroph. J.* **711** (Mar., 2010) 1123–1140.

[12] C. Bischoff, A. Brizius, I. Buder, Y. Chinone, K. Cleary, R. N. Dumoulin, A. Kusaka, R. Monsalve, S. K. Næss, L. B. Newburgh, R. Reeves, K. M. Smith, I. K. Wehus, J. A. Zuntz, J. T. L. Zwart, L. Bronfman, R. Bustos, S. E. Church, C. Dickinson, H. K. Eriksen, P. G. Ferreira, T. Gaier, J. O. Gundersen, M. Hasegawa, M. Hazumi, K. M. Huffenberger, M. E. Jones, P. Kangaslahti, D. J. Kapner, C. R. Lawrence, M. Limon, J. May, J. J. McMahon, A. D. Miller, H. Nguyen, G. W. Nixon, T. J. Pearson, L. Piccirillo, S. J. E. Radford, A. C. S. Readhead, J. L. Richards, D. Samtleben, M. Seiffert, M. C. Shepherd, S. T. Staggs, O. Tajima, K. L. Thompson, K. Vanderlinde, R. Williamson, B. Winstein, and The QUIET Collaboration, *First Season QUIET Observations: Measurements of CMB Polarization Power Spectra at 43 GHz in the Multipole Range* $25 \leq \ell \leq 475$, *ArXiv e-prints* (Dec., 2010) [`arXiv:1012.3191`].

[13] W. J. Percival, B. A. Reid, D. J. Eisenstein, N. A. Bahcall, T. Budavari, J. A. Frieman, M. Fukugita, J. E. Gunn, Ž. Ivezić, G. R. Knapp, R. G. Kron, J. Loveday, R. H. Lupton, T. A. McKay, A. Meiksin, R. C. Nichol, A. C. Pope, D. J. Schlegel, D. P. Schneider, D. N. Spergel, C. Stoughton, M. A. Strauss, A. S. Szalay, M. Tegmark, M. S. Vogeley, D. H. Weinberg, D. G. York, and I. Zehavi, *Baryon acoustic oscillations in the Sloan Digital Sky Survey Data Release 7 galaxy sample*, *Mon. Not. Roy. Astron. Soc.* **401** (Feb., 2010) 2148–2168.

[14] A. G. Riess, L. Macri, S. Casertano, M. Sosey, H. Lampeitl, H. C. Ferguson, A. V. Filippenko, S. W. Jha, W. Li, R. Chornock, and D. Sarkar, *A Redetermination of the Hubble Constant with the Hubble Space Telescope from a Differential Distance Ladder*, *Astroph. J.* **699** (July, 2009) 539–563.

[15] D. Baumann, M. G. Jackson, P. Adshead, A. Amblard, A. Ashoorioon, N. Bartolo, R. Bean, M. Beltrán, F. de Bernardis, S. Bird, X. Chen, D. J. H. Chung, L. Colombo, A. Cooray, P. Creminelli, S. Dodelson, J. Dunkley, C. Dvorkin, R. Easther, F. Finelli, R. Flauger, M. P. Hertzberg, K. Jones-Smith, S. Kachru, K. Kadota, J. Khoury, W. H. Kinney, E. Komatsu,

L. M. Krauss, J. Lesgourgues, A. Liddle, M. Liguori, E. Lim, A. Linde, S. Matarrese, H. Mathur, L. McAllister, A. Melchiorri, A. Nicolis, L. Pagano, H. V. Peiris, M. Peloso, L. Pogosian, E. Pierpaoli, A. Riotto, U. Seljak, L. Senatore, S. Shandera, E. Silverstein, T. Smith, P. Vaudrevange, L. Verde, B. Wandelt, D. Wands, S. Watson, M. Wyman, A. Yadav, W. Valkenburg, and M. Zaldarriaga, *Probing Inflation with CMB Polarization*, in *American Institute of Physics Conference Series* (S. Dodelson, D. Baumann, A. Cooray, J. Dunkley, A. Fraisse, M. G. Jackson, A. Kogut, L. Krauss, M. Zaldarriaga, & K. Smith, ed.), vol. 1141, pp. 10–120, June, 2009.

[16] J.-L. Lehners, *Ekpyrotic and cyclic cosmology*, *Phys. Rep.* **465** (Sept., 2008) 223–263.

[17] L. A. Boyle, P. J. Steinhardt, and N. Turok, *Cosmic gravitational-wave background in a cyclic universe*, *Phys. Rev. D* **69** (June, 2004) 127302–+.

[18] P. A. R. Ade, N. Aghanim, M. Arnaud, M. Ashdown, J. Aumont, C. Baccigalupi, M. Baker, A. Balbi, A. J. Banday, and The *Planck* Collaboration, *Planck Early Results: The Planck mission*, *ArXiv e-prints* (Jan., 2011) [`arXiv:1101.2022`].

[19] G. Efstathiou and S. Gratton, *B-mode detection with an extended* Planck *mission*, *J. Cosmol. Astropart. Phys.* **6** (June, 2009) 11–+.

[20] P. A. R. Ade, N. Aghanim, R. Ansari, M. Arnaud, M. Ashdown, J. Aumont, A. J. Banday, M. Bartelmann, J. G. Bartlett, and The *Planck* HFI Core Team, Planck *early results. IV. First assessment of the High Frequency Instrument in-flight performance*, *Astron. Astroph.* **536** (Dec., 2011) A4, [`arXiv:1101.2039`].

[21] J. P. Filippini, P. A. R. Ade, M. Amiri, S. J. Benton, R. Bihary, J. J. Bock, J. R. Bond, J. A. Bonetti, S. A. Bryan, B. Burger, H. C. Chiang, C. R. Contaldi, B. P. Crill, O. Doré, M. Farhang, L. M. Fissel, N. N. Gandilo, S. R. Golwala, J. E. Gudmundsson, M. Halpern, M. Hasselfield, G. Hilton, W. Holmes, V. V. Hristov, K. D. Irwin, W. C. Jones, C. L. Kuo, C. J. MacTavish, P. V. Mason, T. E. Montroy, T. A. Morford, C. B. Netterfield, D. T. O'Dea, A. S. Rahlin, C. D. Reintsema, J. E. Ruhl, M. C. Runyan, M. A. Schenker, J. A. Shariff, J. D. Soler, A. Trangsrud, C. Tucker, R. S. Tucker, and A. D. Turner, *SPIDER: a balloon-borne CMB polarimeter for large angular scales*, in *Society of Photo-Optical Instrumentation Engineers (SPIE) Conference Series*, vol. 7741, July, 2010.

[22] C. L. Kuo, J. J. Bock, J. A. Bonetti, J. Brevik, G. Chattopadhyay, P. K. Day, S. Golwala, M. Kenyon, A. E. Lange, H. G. LeDuc, H. Nguyen, R. W. Ogburn, A. Orlando, A. Transgrud, A. Turner, G. Wang, and J. Zmuidzinas, *Antenna-coupled TES bolometer arrays for CMB polarimetry*, in *Society of Photo-Optical Instrumentation Engineers (SPIE) Conference Series*, vol. 7020, Aug., 2008.

[23] P. A. J. de Korte, J. Beyer, S. Deiker, G. C. Hilton, K. D. Irwin, M. Macintosh, S. W. Nam, C. D. Reintsema, L. R. Vale, and M. E. Huber, *Time-division superconducting quantum interference device multiplexer for transition-edge sensors*, *Rev. Sci. Instr.* **74** (Aug., 2003) 3807–3815.

[24] E. Battistelli et al., *Functional description of read-out electronics for time-domain multiplexed bolometers for millimeter and sub-millimeter astronomy*, *Journal of Low Temperature Physics* **151** (2008), no. 3-4 908–914.

[25] R. W. Ogburn, IV, P. A. R. Ade, R. W. Aikin, M. Amiri, S. J. Benton, J. J. Bock, J. A. Bonetti, J. A. Brevik, B. Burger, C. D. Dowell, L. Duband, J. P. Filippini, S. R. Golwala, M. Halpern, M. Hasselfield, G. Hilton, V. V. Hristov, K. Irwin, J. P. Kaufman, B. G. Keating, J. M. Kovac, C. L. Kuo, A. E. Lange, E. M. Leitch, C. B. Netterfield, H. T. Nguyen, A. Orlando, C. L. Pryke, C. Reintsema, S. Richter, J. E. Ruhl, M. C. Runyan, C. D. Sheehy, Z. K. Staniszewski, S. A. Stokes, R. V. Sudiwala, G. P. Teply, J. E. Tolan, A. D. Turner, P. Wilson, and C. L. Wong, *The BICEP2 CMB polarization experiment*, in *Society of Photo-Optical Instrumentation Engineers (SPIE) Conference Series*, vol. 7741, July, 2010.

[26] C. D. Sheehy, P. A. R. Ade, R. W. Aikin, M. Amiri, S. Benton, C. Bischoff, J. J. Bock, J. A. Bonetti, J. A. Brevik, B. Burger, C. D. Dowell, L. Duband, J. P. Filippini, S. R. Golwala, M. Halpern, M. Hasselfield, G. Hilton, V. V. Hristov, K. Irwin, J. P. Kaufman, B. G. Keating, J. M. Kovac, C. L. Kuo, A. E. Lange, E. M. Leitch, M. Lueker, C. B. Netterfield, H. T. Nguyen, R. W. Ogburn, IV, A. Orlando, C. L. Pryke, C. Reintsema, S. Richter, J. E. Ruhl, M. C. Runyan, Z. Staniszewski, S. Stokes, R. Sudiwala, G. Teply, K. L. Thompson, J. E. Tolan, A. D. Turner, P. Wilson, and C. L. Wong, *The Keck Array: a pulse tube cooled CMB polarimeter*, in *Society of Photo-Optical Instrumentation Engineers (SPIE) Conference Series*, vol. 7741, July, 2010.

[27] J. R. Pardo, J. Cernicharo, and E. Serabyn, *Atmospheric transmission at microwaves (ATM): an improved model for millimeter/submillimeter applications*, *IEEE Transactions on Antennas and Propagation* **49** (Dec., 2001) 1683–1694.

[28] E. Pascale, P. A. R. Ade, J. J. Bock, E. L. Chapin, J. Chung, M. J. Devlin, S. Dicker, M. Griffin, J. O. Gundersen, M. Halpern, P. C. Hargrave, D. H. Hughes, J. Klein, C. J. MacTavish, G. Marsden, P. G. Martin, T. G. Martin, P. Mauskopf, C. B. Netterfield, L. Olmi, G. Patanchon, M. Rex, D. Scott, C. Semisch, N. Thomas, M. D. P. Truch, C. Tucker, G. S. Tucker, M. P. Viero, and D. V. Wiebe, *The Balloon-borne Large Aperture Submillimeter Telescope: BLAST*, *Astroph. J.* **681** (July, 2008) 400–414.

[29] S. Masi, P. A. R. Ade, J. J. Bock, J. R. Bond, J. Borrill, A. Boscaleri, P. Cabella, C. R. Contaldi, B. P. Crill, P. de Bernardis, G. de Gasperis, A. de Oliveira-Costa, G. de Troia, G. di Stefano, P. Ehlers, E. Hivon, V. Hristov, A. Iacoangeli, A. H. Jaffe, W. C. Jones, T. S. Kisner, A. E. Lange, C. J. MacTavish, C. Marini Bettolo, P. Mason, P. D. Mauskopf, T. E. Montroy, F. Nati, L. Nati, P. Natoli, C. B. Netterfield, E. Pascale, F. Piacentini, D. Pogosyan, G. Polenta, S. Prunet, S. Ricciardi, G. Romeo, J. E. Ruhl, P. Santini, M. Tegmark, E. Torbet, M. Veneziani, and N. Vittorio, *Instrument, method, brightness, and polarization maps from the 2003 flight of BOOMERanG*, *Astron. Astroph.* **458** (Nov., 2006) 687–716.

[30] S. A. Bryan, P. A. R. Ade, M. Amiri, S. Benton, R. Bihary, J. J. Bock, J. R. Bond, J. A. Bonetti, H. C. Chiang, C. R. Contaldi, B. P. Crill, D. O'Dea, O. Dore, M. Farhang, J. P. Filippini, L. Fissel, N. Gandilo, S. Golwala, J. E. Gudmundsson, M. Hasselfield, M. Halpern, K. R. Helson, G. Hilton, W. Holmes, V. V. Hristov, K. D. Irwin, W. C. Jones, C. L. Kuo, C. J. MacTavish, P. Mason, T. Morford, T. E. Montroy, C. B. Netterfield, A. S. Rahlin, C. D. Reintsema, D. Riley, J. E. Ruhl, M. C. Runyan, M. A. Schenker, J. Shariff, J. D. Soler, A. Transrud, R. Tucker, C. Tucker, and A. Turner, *Modeling and characterization of the SPIDER half-wave plate*, in *Society of Photo-Optical Instrumentation Engineers (SPIE) Conference Series*, vol. 7741, July, 2010.

[31] M. C. Runyan, P. A. R. Ade, M. Amiri, S. Benton, R. Bihary, J. J. Bock, J. R. Bond, J. A. Bonetti, S. A. Bryan, H. C. Chiang, C. R. Contaldi, B. P. Crill, O. Dore, D. O'Dea, M. Farhang, J. P. Filippini, L. Fissel, N. Gandilo, S. R. Golwala, J. E. Gudmundsson, M. Hasselfield, M. Halpern, G. Hilton, W. Holmes, V. V. Hristov, K. D. Irwin, W. C. Jones, C. L. Kuo, C. J. MacTavish, P. V. Mason, T. A. Morford, T. E. Montroy, C. B. Netterfield, A. S. Rahlin, C. D. Reintsema, J. E. Ruhl, M. A. Schenker, J. Shariff, J. D. Soler, A. Trangsrud, R. S. Tucker, C. E. Tucker, and A. Turner, *Design and performance of the SPIDER instrument*, in *Society of Photo-Optical Instrumentation Engineers (SPIE) Conference Series*, vol. 7741, July, 2010.

[32] J. E. Gudmundsson, P. A. R. Ade, M. Amiri, S. J. Benton, R. Bihary, J. J. Bock, J. R. Bond, J. A. Bonetti, S. A. Bryan, B. Burger, H. C. Chiang, C. R. Contaldi, B. P. Crill, O. Doré, M. Farhang, J. Filippini, L. M. Fissel, N. N. Gandilo, S. R. Golwala, M. Halpern, M. Hasselfield, G. Hilton, W. Holmes, V. V. Hristov, K. D. Irwin, W. C. Jones, C. L. Kuo, C. J. MacTavish, P. V. Mason, T. E. Montroy, T. A. Morford, C. B. Netterfield, D. T. O'Dea, A. S. Rahlin, C. D. Reintsema, J. E. Ruhl, M. C. Runyan, M. A. Schenker, J. A. Shariff, J. D. Soler, A. Trangsrud, C. Tucker, R. S. Tucker, and A. D. Turner, *Thermal architecture for the*

SPIDER flight cryostat, in *Society of Photo-Optical Instrumentation Engineers (SPIE) Conference Series*, vol. 7741, July, 2010.

[33] D. T. O'Dea, P. A. R. Ade, M. Amiri, S. J. Benton, J. J. Bock, J. R. Bond, J. A. Bonetti, S. Bryan, B. Burger, H. C. Chiang, C. N. Clark, C. R. Contaldi, B. P. Crill, G. Davis, O. Dore, M. Farhang, J. P. Filippini, L. M. Fissel, A. A. Fraisse, N. N. Gandilo, S. Golwala, J. E. Gudmundsson, M. Hasselfield, G. Hilton, W. Holmes, V. V. Hristov, K. Irwin, W. C. Jones, C. L. Kuo, C. J. MacTavish, P. V. Mason, T. E. Montroy, T. A. Morford, C. B. Netterfield, A. S. Rahlin, C. Reintsema, J. E. Ruhl, M. C. Runyan, M. A. Schenker, J. A. Shariff, J. D. Soler, A. Trangsrud, C. Tucker, R. S. Tucker, A. D. Turner, and D. Wiebe, *Spider Optimization II: Optical, Magnetic and Foreground Effects*, *ArXiv e-prints* (Feb., 2011) [arXiv:1102.0559].

[34] Y. D. Takahashi, P. A. R. Ade, D. Barkats, J. O. Battle, E. M. Bierman, J. J. Bock, H. C. Chiang, C. D. Dowell, L. Duband, E. F. Hivon, W. L. Holzapfel, V. V. Hristov, W. C. Jones, B. G. Keating, J. M. Kovac, C. L. Kuo, A. E. Lange, E. M. Leitch, P. V. Mason, T. Matsumura, H. T. Nguyen, N. Ponthieu, C. Pryke, S. Richter, G. Rocha, and K. W. Yoon, *Characterization of the BICEP Telescope for High-precision Cosmic Microwave Background Polarimetry*, *Astroph. J.* **711** (Mar., 2010) 1141–1156.

[35] W. C. Jones, P. A. R. Ade, J. J. Bock, J. R. Bond, J. Borrill, A. Boscaleri, P. Cabella, C. R. Contaldi, B. P. Crill, P. de Bernardis, G. de Gasperis, A. de Oliveira-Costa, G. de Troia, G. di Stefano, E. Hivon, A. H. Jaffe, T. S. Kisner, A. E. Lange, C. J. MacTavish, S. Masi, P. D. Mauskopf, A. Melchiorri, T. E. Montroy, P. Natoli, C. B. Netterfield, E. Pascale, F. Piacentini, D. Pogosyan, G. Polenta, S. Prunet, S. Ricciardi, G. Romeo, J. E. Ruhl, P. Santini, M. Tegmark, M. Veneziani, and N. Vittorio, *Observations of the temperature and polarization anisotropies with BOOMERANG 2003*, *New Astron. Rev.* **50** (Dec., 2006) 945–950.

[36] R. W. Aikin, P. A. Ade, S. Benton, J. J. Bock, J. A. Bonetti, J. A. Brevik, C. D. Dowell, L. Duband, J. P. Filippini, S. R. Golwala, M. Halpern, V. V. Hristov, K. Irwin, J. P. Kaufman, B. G. Keating, J. M. Kovac, C. L. Kuo, A. E. Lange, C. B. Netterfield, H. T. Nguyen, R. W. Ogburn, IV, A. Orlando, C. Pryke, S. Richter, J. E. Ruhl, M. C. Runyan, C. Sheehy, S. A. Stokes, R. Sudiwala, G. P. Teply, J. E. Tolan, A. D. Turner, P. Wilson, and C. L. Wong, *Optical performance of the BICEP2 Telescope at the South Pole*, in *Society of Photo-Optical Instrumentation Engineers (SPIE) Conference Series*, vol. 7741, July, 2010.

[37] C. J. MacTavish, P. A. R. Ade, E. S. Battistelli, S. Benton, R. Bihary, J. J. Bock, J. R. Bond, J. Brevik, S. Bryan, C. R. Contaldi, B. P. Crill, O. Doré, L. Fissel, S. R. Golwala, M. Halpern, G. Hilton, W. Holmes, V. V. Hristov, K. Irwin, W. C. Jones, C. L. Kuo, A. E. Lange, C. Lawrie, T. G. Martin, P. Mason, T. E. Montroy, C. B. Netterfield, D. Riley, J. E. Ruhl, M. Runyan, A. Trangsrud, C. Tucker, A. Turner, M. Viero, and D. Wiebe, *Spider Optimization: Probing the Systematics of a Large-Scale B-Mode Experiment*, *Astroph. J.* **689** (Dec., 2008) 655–665.

[38] J. Bock, A. Cooray, S. Hanany, B. Keating, A. Lee, T. Matsumura, M. Milligan, N. Ponthieu, T. Renbarger, and H. Tran, *The Experimental Probe of Inflationary Cosmology (EPIC): A Mission Concept Study for NASA's Einstein Inflation Probe*, *ArXiv e-prints* (May, 2008) [arXiv:0805.4207].

[39] J. Dunkley, A. Amblard, C. Baccigalupi, M. Betoule, D. Chuss, A. Cooray, J. Delabrouille, C. Dickinson, G. Dobler, J. Dotson, H. K. Eriksen, D. Finkbeiner, D. Fixsen, P. Fosalba, A. Fraisse, C. Hirata, A. Kogut, J. Kristiansen, C. Lawrence, A. M. Magalhães, M. A. Miville-Deschenes, S. Meyer, A. Miller, S. K. Naess, L. Page, H. V. Peiris, N. Phillips, E. Pierpaoli, G. Rocha, J. E. Vaillancourt, and L. Verde, *Prospects for polarized foreground removal*, in *American Institute of Physics Conference Series* (S. Dodelson, D. Baumann, A. Cooray, J. Dunkley, A. Fraisse, M. G. Jackson, A. Kogut, L. Krauss, M. Zaldarriaga, & K. Smith, ed.), vol. 1141, pp. 222–264, June, 2009.

[40] J. Cho and A. Lazarian, *Galactic Foregrounds: Spatial Fluctuations and a Procedure for Removal*, Astroph. J. **720** (Sept., 2010) 1181–1201.

[41] D. P. Finkbeiner, M. Davis, and D. J. Schlegel, *Extrapolation of Galactic Dust Emission at 100 Microns to Cosmic Microwave Background Radiation Frequencies Using FIRAS*, Astroph. J. **524** (Oct., 1999) 867–886.

[42] A. Lazarian and D. Finkbeiner, *Microwave emission from aligned dust*, New Astron. Rev. **47** (Dec., 2003) 1107–1116.

[43] G. B. Rybicki and A. P. Lightman, *Radiative Processes in Astrophysics*. New York, Wiley, 1979.

[44] W. A. Hiltner, *Polarization of Light from Distant Stars by Interstellar Medium*, Science **109** (Feb., 1949) 165.

[45] J. S. Hall, *Observations of the Polarized Light from Stars*, Science **109** (Feb., 1949) 166–167.

[46] T. Hoang and A. Lazarian, *Radiative torque alignment: essential physical processes*, Mon. Not. Roy. Astron. Soc. **388** (July, 2008) 117–143.

[47] A. Benoît, P. Ade, A. Amblard, R. Ansari, É. Aubourg, S. Bargot, J. G. Bartlett, J.-P. Bernard, R. S. Bhatia, A. Blanchard, J. J. Bock, A. Boscaleri, F. R. Bouchet, A. Bourrachot, P. Camus, F. Couchot, P. de Bernardis, J. Delabrouille, F.-X. Désert, O. Doré, M. Douspis, L. Dumoulin, X. Dupac, P. Filliatre, P. Fosalba, K. Ganga, F. Gannaway, B. Gautier, M. Giard, Y. Giraud-Héraud, R. Gispert, L. Guglielmi, J.-C. Hamilton, S. Hanany, S. Henrot-Versillé, J. Kaplan, G. Lagache, J.-M. Lamarre, A. E. Lange, J. F. Macías-Pérez, K. Madet, B. Maffei, C. Magneville, D. P. Marrone, S. Masi, F. Mayet, A. Murphy, F. Naraghi, F. Nati, G. Patanchon, G. Perrin, M. Piat, N. Ponthieu, S. Prunet, J.-L. Puget, C. Renault, C. Rosset, D. Santos, A. Starobinsky, I. Strukov, R. V. Sudiwala, R. Teyssier, M. Tristram, C. Tucker, J.-C. Vanel, D. Vibert, E. Wakui, and D. Yvon, *First detection of polarization of the submillimetre diffuse galactic dust emission by Archeops*, Astron. Astroph. **424** (Sept., 2004) 571–582.

[48] B. T. Draine and A. A. Fraisse, *Polarized Far-Infrared and Submillimeter Emission from Interstellar Dust*, Astroph. J. **696** (May, 2009) 1–11.

[49] B. T. Draine, *Physics of the Interstellar and Intergalactic Medium*. Princeton University Press, 2011.

[50] A. Kogut, J. Dunkley, C. L. Bennett, O. Doré, B. Gold, M. Halpern, G. Hinshaw, N. Jarosik, E. Komatsu, M. R. Nolta, N. Odegard, L. Page, D. N. Spergel, G. S. Tucker, J. L. Weiland, E. Wollack, and E. L. Wright, *Three-Year Wilkinson Microwave Anisotropy Probe (WMAP) Observations: Foreground Polarization*, Astroph. J. **665** (Aug., 2007) 355–362.

[51] E. Hivon, K. M. Górski, C. B. Netterfield, B. P. Crill, S. Prunet, and F. Hansen, *MASTER of the Cosmic Microwave Background Anisotropy Power Spectrum: A Fast Method for Statistical Analysis of Large and Complex Cosmic Microwave Background Data Sets*, Astroph. J. **567** (Mar., 2002) 2–17.

[52] W. C. Jones, T. E. Montroy, B. P. Crill, C. R. Contaldi, T. S. Kisner, A. E. Lange, C. J. MacTavish, C. B. Netterfield, and J. E. Ruhl, *Instrumental and analytic methods for bolometric polarimetry*, Astron. Astroph. **470** (Aug., 2007) 771–785.

[53] W. C. Jones, P. A. R. Ade, J. J. Bock, J. R. Bond, J. Borrill, A. Boscaleri, P. Cabella, C. R. Contaldi, B. P. Crill, P. de Bernardis, G. De Gasperis, A. de Oliveira-Costa, G. De Troia, G. di Stefano, E. Hivon, A. H. Jaffe, T. S. Kisner, A. E. Lange, C. J. MacTavish, S. Masi, P. D. Mauskopf, A. Melchiorri, T. E. Montroy, P. Natoli, C. B. Netterfield, E. Pascale, F. Piacentini, D. Pogosyan, G. Polenta, S. Prunet, S. Ricciardi, G. Romeo, J. E. Ruhl, P. Santini, M. Tegmark, M. Veneziani, and N. Vittorio, *A Measurement of the Angular Power Spectrum of the CMB Temperature Anisotropy from the 2003 Flight of BOOMERANG*, Astroph. J. **647** (Aug., 2006) 823–832.

[54] B. Gold, C. L. Bennett, R. S. Hill, G. Hinshaw, N. Odegard, L. Page, D. N. Spergel, J. L. Weiland, J. Dunkley, M. Halpern, N. Jarosik, A. Kogut, E. Komatsu, D. Larson, S. S. Meyer, M. R. Nolta, E. Wollack, and E. L. Wright, *Five-Year Wilkinson Microwave Anisotropy Probe Observations: Galactic Foreground Emission*, Astroph. J. Suppl. **180** (Feb., 2009) 265–282.

[55] D. Larson, J. Dunkley, G. Hinshaw, E. Komatsu, M. R. Nolta, C. L. Bennett, B. Gold, M. Halpern, R. S. Hill, N. Jarosik, A. Kogut, M. Limon, S. S. Meyer, N. Odegard, L. Page, K. M. Smith, D. N. Spergel, G. S. Tucker, J. L. Weiland, E. Wollack, and E. L. Wright, *Seven-year Wilkinson Microwave Anisotropy Probe (WMAP) Observations: Power Spectra and WMAP-derived Parameters*, Astroph. J. Suppl. **192** (Feb., 2011) 16–+.

[56] C. Armitage-Caplan, J. Dunkley, H. K. Eriksen, and C. Dickinson, *Impact on the tensor-to-scalar ratio of incorrect Galactic foreground modelling*, Mon. Not. Roy. Astron. Soc. **424** (Aug., 2012) 1914–1924, [`arXiv:1203.0152`].

[57] K. M. Górski, E. Hivon, A. J. Banday, B. D. Wandelt, F. K. Hansen, M. Reinecke, and M. Bartelmann, *HEALPix: A Framework for High-Resolution Discretization and Fast Analysis of Data Distributed on the Sphere*, Astroph. J. **622** (Apr., 2005) 759–771.

[58] M. Frigo and S. G. Johnson, *The Design and Implementation of FFTW3*, Proc. IEEE **93** (2005) 216.